Thesis for the degree of Doctor of Philosophy

The impact of mesospheric dynamics and chemistry on key chemical species: 20 years of Odin/SMR satellite observations

Francesco Grieco

Department of Space, Earth and Environment
CHALMERS UNIVERSITY OF TECHNOLOGY
Göteborg, Sweden 2022

The impact of mesospheric dynamics and chemistry on key chemical species: 20 years of Odin/SMR satellite observations
Francesco Grieco

Doktorsavhandlingar vid Chalmers tekniska högskola
Ny serie nr 5221
ISBN 978-91-7905-755-8

Department of Space, Earth and Environment
Chalmers University of Technology
SE–412 96 Göteborg, Sweden
Telephone + 46 (0) 31 – 772 1000

Front cover image: Silhouette of the space shuttle Endeavour straddling the stratosphere (white) and the mesosphere (blue). Image credit: NASA
Back cover image: a picture of the author taken by his talented friend Eden Rafealov.

Typeset by the author using LaTeX.

Printed by Chalmers Reproservice
Göteborg, Sweden 2022

Abstract

Coupling mechanisms between different atmospheric layers are such that changes in middle atmospheric dynamics and composition have an effect on what happens at lower altitudes and on the climate. There is therefore a need to extend climate models to include higher altitudes and to perform measurements of the middle atmosphere. Carbon monoxide (CO), water vapour (H_2O) and nitric oxide (NO) are species of high scientific interest due to their aptness to being used as circulation tracers in the middle atmosphere, due to their long photochemical lifetime (for NO, this is only true during polar winter). Moreover, NO plays a decisive role for ozone (O_3) chemistry. In fact, the downward branch of the middle atmospheric residual circulation is responsible for the descent of NO generated by energetic particle precipitation (EPP) in the mesosphere and lower thermosphere (MLT) to lower altitudes where it is involved in catalytic destruction of O_3. However, the estimates on the amount of EPP NO thus descending still present large uncertainties. In addition to this, NO observations allow us to estimate its oscillation in concentration due to atmospheric solar tides in the middle atmosphere. Among the satellite instruments currently performing remote sensing of the middle atmosphere, the Sub-Millimetre Radiometer (SMR) on board the Odin satellite is one of the most long-lived. SMR has indeed been performing limb sounding of the middle atmosphere for 21 years. However, the CO and H_2O data sets are both affected by instrumental artifacts that resulted in a misestimation of the two species' concentration and, in the case of CO, also caused failure of the retrieval process. Papers 1 and 2 included in this thesis focus on identifying the causes and correcting such artifacts, leading to two new long-term and global data sets that are now available to the scientific community to study middle atmospheric dynamics. In Paper 3, high latitude mesospheric NO observations from SMR were used to measure the flux of EPP NO transported down through the mesosphere during each polar winter, in both hemispheres. Such collection of EPP NO mesospheric fluxes is unique - considering the longevity of Odin/SMR and that it is the only instrument currently observing mesospheric NO globally. It can help reduce the uncertainties in the above mentioned estimates of descending EPP NO, providing the possibility to further study the impact of EPP on the atmosphere. Finally, the SMR NO data set was also used in Paper 4 with the aim of investigating the tidal signature in lower thermospheric NO concentration at low latitudes, with a particular focus on how NO diurnal variations are affected by nonmigrating semidiurnal atmospheric solar tides.

Keywords: microwave limb sounding, mesosphere, CO, H_2O, NO, energetic particle precipitation, atmospheric solar tides.

Acknowledgments

I would like to thank my supervisors Kristell Pérot and Donal Murtagh for their inspiring dedication towards their job as scientists, for their kindness and friendliness, and for always being ready to provide their precious guidance when needed.

Thanks to Patrick Eriksson for his contribution to the supervision of my work and for guiding me in the use of ARTS. Thanks to Yvan Orsolini for the fruitful discussions and for the great support provided during the last months of my PhD. Thanks to Bengt Rydberg and Joakim Möller from Molflow for their readiness in providing assistance with issues in processing Odin/SMR data.

Finally, I would like to thank Sandra, my family and my friends, both old and new, for making the journey that took to the completion of this thesis more gentle with their endless support and love.

Francesco Grieco
Göteborg, November 2022

List of Publications

This thesis is based on the following appended papers:

Paper 1. Francesco Grieco, Kristell Pérot, Donal Murtagh, Patrick Eriksson, Peter Forkman, Bengt Rydberg, Bernd Funke, Kaley A. Walker, and Hugh C. Pumphrey. *Recovery and validation of Odin/SMR long term measurements of mesospheric carbon monoxide.* Atmospheric Measurement Techniques, 13, 5013–5031, https://doi.org/10.5194/amt-13-5013-2020,
Published: 25 September 2020.

Paper 2. Francesco Grieco, Kristell Pérot, Donal Murtagh, Patrick Eriksson, Bengt Rydberg, Michael Kiefer, Maya Garcia-Comas, Alyn Lambert, and Kaley A. Walker. *Improvement of Odin/SMR water vapour measurements and validation of the obtained dataset.* Atmospheric Measurement Techniques, 14, 5823–5857, https://doi.org/10.5194/amt-14-5823-2021,
Published: 27 August 2021.

Paper 3. Francesco Grieco, Kristell Pérot, Donal Murtagh. *Long-term mesospheric record of EPP-IE NO measured by Odin/SMR.* Journal of Atmospheric and Solar-Terrestrial Physics,
Available at SSRN: https://ssrn.com/abstract=4160670,
Under review.

Paper 4. Francesco Grieco, Yvan Orsolini, Kristell Pérot. *Semidiurnal nonmigrating tides in low-latitude lower thermospheric NO: a climatology based on 20 years of Odin/SMR measurements.* Manuscript in preparation.

Contents

Part I

Introductory chapters

Chapter 1

Introduction

The Earth's atmosphere can be divided into altitude regions according to different criteria. A common way to do this is to divide the atmosphere in regions characterised by different temperature gradients, with divisions placed in correspondence of reversals of the gradient (Brasseur et al., 2005). Thus four layers are defined, from bottom to top: troposphere, stratosphere, mesosphere and thermosphere (see Figure 1.1). The troposphere ranges from the surface to about 8 km at the poles and to about 17 km at the equator. This layer is characterised by a mean vertical temperature gradient of -6.5 K/km to reach approximately 200 K at the equator and 230 K at the summer pole. These temperatures are reached at the tropopause, i.e. where the gradient reverses. On top of it there is the stratosphere which extends up to 50 km altitude. In this region, the temperature increases with altitude due to the absorption of ultraviolet solar radiation by the ozone layer, which represents approximately 90% of all ozone present in the atmosphere. At around 50 km is the stratopause and above it there is the mesosphere where temperature decreases with altitude by about 3 ± 1 K/km. A temperature minimum is reached at the mesopause which is observed at different altitudes depending on the location and time of the year: $\sim$95 km at the equator, with a minimum temperature of $\sim$170 K; $\sim$88 km at the summer pole with temperature $\sim$130 K. The uppermost layer is the thermosphere where the temperature increases rapidly with altitude to reach temperatures above 1500 K. There, the gas density is so low and collisions so infrequent that the species are distributed within different altitudes based on their atomic weights. Moreover, in the thermosphere, energetic ultraviolet and X-ray photons from the sun are responsible for ionisation and dissociation of molecules. Thus, the constituents are mainly atomic oxygen (O), atomic nitrogen (N), and helium (He).

The lower part of the atmosphere, the one where we live and where weather happens, has been object of studies for centuries. However, it was only during the last 40 years that the region between $\sim$10 and 100 km altitude - including the stratosphere, the mesosphere and the lower thermosphere - could be investigated, thanks to the development of various types of instruments placed on board balloons, airplanes, rockets and satellites, performing measurements that were not possible before. This region is often referred to as middle atmosphere. Observations in this

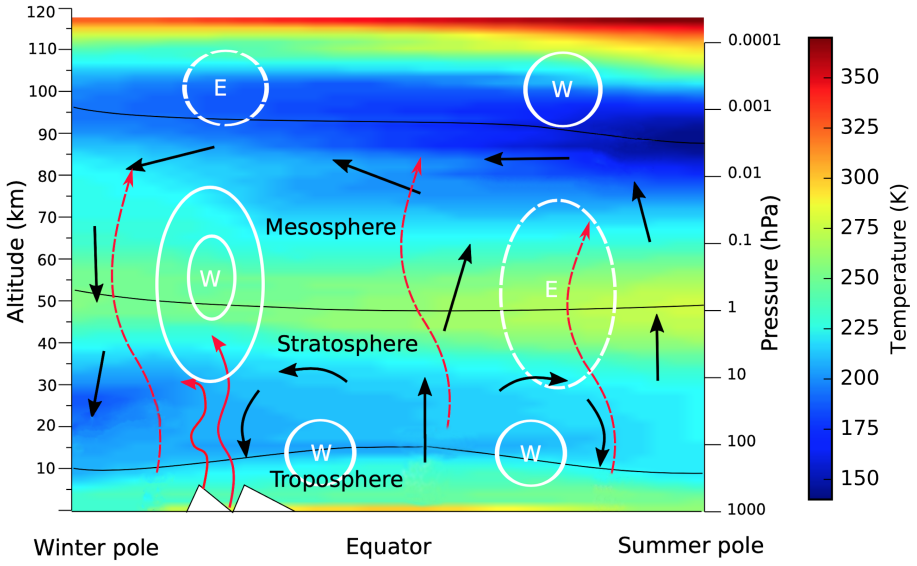

Figure 1.1: Summary picture of circulation in the atmosphere until 120 km altitude, and temperature distribution at the solstice (background colours). White lines represent zonal winds, i.e. westerlies (W) and easterlies (E); dashed and solid red arrows represent the direction of propagation of gravity and Rossby waves respectively; black arrows represent the mean meridional circulation. Figure credit: O.M. Christensen and M.R. Schoeberl.

altitude region are necessary in order to study the atmospheric system as a whole. Some of the knowledge that has been acquired about middle atmospheric dynamics is summarised in Chapter 3.

External perturbations affect the middle atmosphere: photochemical dissociation and ionisation of molecules by solar radiation become more important with increasing altitude, so species at higher altitudes are more subject to solar variability; at low altitudes instead, middle atmospheric composition is influenced by volcanic eruptions and anthropogenic emissions taking place in the troposphere. One can then see how the middle atmosphere composition is influenced by what happens both above and below it. Its dynamics is also heavily determined by tropospheric dynamics (see Section 3.1) and atmospheric tides that originate in the troposphere propagate upwards and connect all the layers of the atmosphere (see Section 3.2). On the other hand, what happens in the middle atmosphere affects lower altitudes, and thus us: for example, the ozone layer is located in the middle atmosphere, absorbing 250-300 nm ultraviolet solar radiation and protecting life on Earth from being exposed to such radiation. Changes in middle atmospheric ozone concentration can also affect the thermal structure of this region and its dynamics, which in turn affect the climate variability at the surface via coupling phenomena (e.g., Rozanov et al., 2012; Seppälä et al., 2014). Moreover, water vapour (H_2O) is one of the most important greenhouse gases in the middle atmosphere. Changes in its concentration can therefore have a significant impact on global climate (see Section 2.2). Because of these mutual influences between the middle atmosphere and other layers, in particular because of

the impact of the middle atmosphere on the troposphere and hence on climate, it is very important to observe it. A better understanding of the processes going on in the middle atmosphere will allow us to extend the upper limit of climate models and therefore obtain more accurate climate forecasts. In fact, for a long time, the lower atmosphere was the only region taken into account in climate models but, due to the increasing realisation of interdependence between different layers, high-top models are now thought to be necessary to obtain more accurate climate forecast (Gerber et al., 2012; Marsh et al., 2013). The models used for IPCC (Intergovernmental Panel on Climate Change) climate assessments used to consider only altitudes up till 30 km in 2001 while today they reach up to 80 km and, in the future, they should cover the upper mesosphere and lower thermosphere.

Molecules undergo three different kinds of energy transition: electronic, vibrational and rotational. An electron of a molecule de-exciting from a higher energy state to a lower one, i.e. passing from a higher to a lower orbit, emits radiation in the ultraviolet and visible range. Lower energy transitions occur when the molecule goes from a vibrational state which is higher - faster vibration - to a lower one - slower vibration -, resulting in emission of infrared radiation. Finally, even lower energies are involved for transitions between rotational states, with emission of radiation in the millimetre and sub-millimetre spectral regions. In the Earth's atmosphere, radiance from molecular emission dominates over solar radiance in the infrared and millimetre/sub-millimetre spectral regions, thus observations of the atmosphere at these wavelengths allow to retrieve molecules' concentration and temperature. Keeping track of how these change in time and space is a precious source of information about the dynamics and chemical processes occurring. Spaceborne radiometers allow to perform such measurements on a global scale, and the Sub-Millimetre Radiometer (SMR) on board the Odin satellite is one of them (described in Chapter 5). It has been operating for over 21 years and still is today. That is a very long life if one considers that the mission was originally supposed to last 2 years. This particularly long operational period makes the Odin products very valuable for atmospheric science studies (see Figure 1.2).

However, the products of the observations relative to some species, including carbon monoxide (CO) and water vapour (H_2O), were subject to instrumental artifacts and were unusable, as in the case of CO, or presenting important biases, as in the case of H_2O. To make these long term data sets usable, the effects of the instrumental issues have been quantified and corrected. The work done to achieve this result constitutes the subject of Papers 1 and 2 included in this thesis. New retrievals from the corrected spectra have been performed and a description of the retrieval process is presented in Section 5.5.

Among other species, Odin/SMR also measures nitric oxide (NO) and is today the only instrument measuring this chemical species globally in the mesosphere. The other 2 papers included in the thesis are based on SMR NO observations which, in Paper 3, were used to quantify the flux of NO generated from energetic particle precipitation (EPP; see Chapter 4) descending through the mesosphere during polar winter, whereas in Paper 4 allowed to quantify the oscillation in NO mixing ratio due to semidiurnal nonmigrating tides (see Section 3.2) in the lower thermosphere at

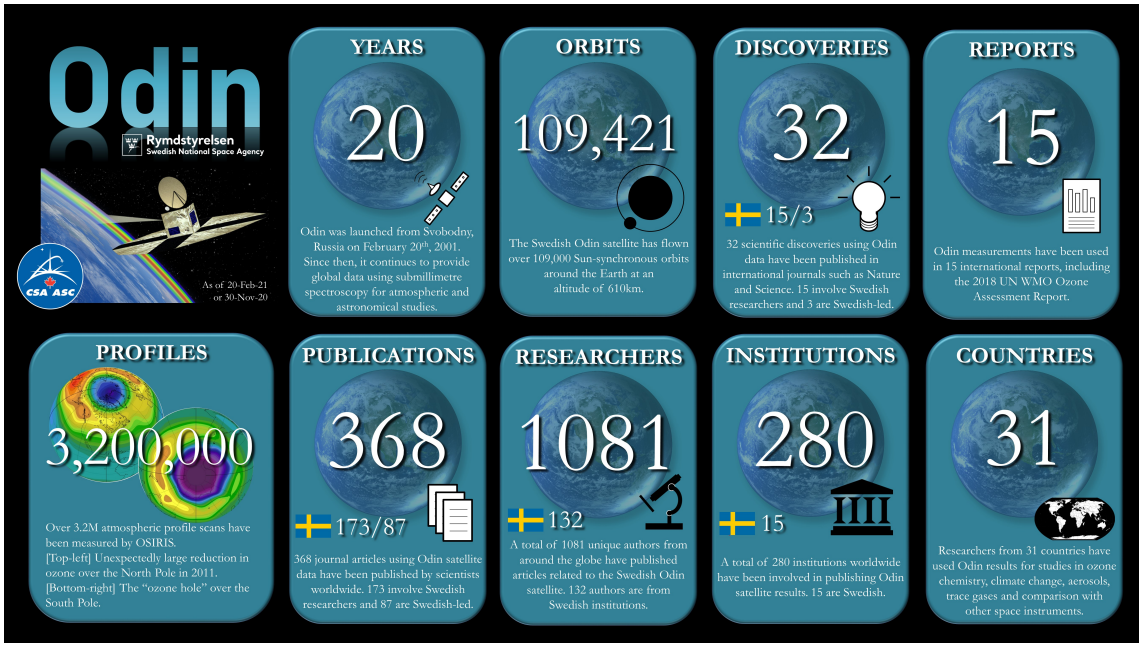

Figure 1.2: Infographics summarising achievements of Odin/SMR and Odin/OSIRIS altogether. Figure credit: Canadian Space Agency.

low latitudes. All mentioned papers are summarised in Chapter 6.

Chapter 2

Middle atmospheric chemistry

In this chapter, an overview of the main reactions involving the chemical species studied in the appended papers - that is middle atmospheric CO, H_2O and NO - is presented.

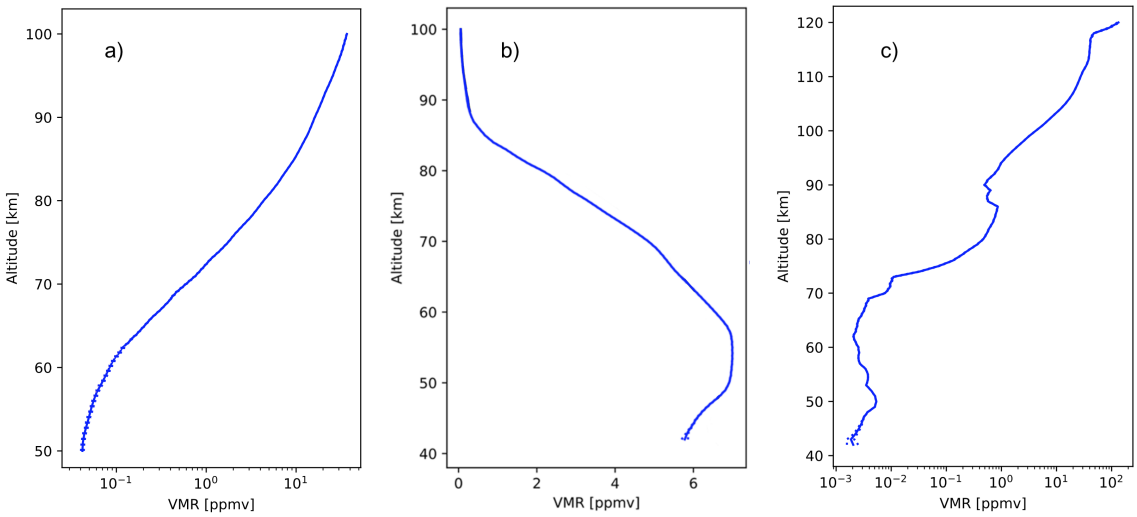

Figure 2.1: Mesospheric concentration profiles of CO (a), H_2O (b) and NO (c) retrieved from SMR observations. The data are averaged globally and over the whole SMR operational period. The dashed lines represent the standard deviation of the median which, in some cases, is smaller than the thickness of the profile line, causing the dashed line not to be distinguishable. Note the different scales on both x- and y-axis.

2.1 CO chemistry

Tropospheric CO has both anthropogenic (e.g. industrial activities, biomass burning, transport and heating) and natural sources. However, very little of this CO reaches the stratosphere, due to reaction with the hydroxyl radical (OH):

$$CO + OH \rightarrow CO_2 + H. \tag{2.1}$$

For this reason, very little of it reaches the stratosphere (Zander et al., 1981). The carbon monoxide which is present in the middle atmosphere is produced mainly via methane (CH_4) oxidation, through the following reactions:

$$CH_4 + OH \rightarrow CO + products, \tag{2.2}$$

$$CH_4 + Cl \rightarrow CO + products, \tag{2.3}$$

$$CH_4 + O(^1D) \rightarrow CO + products; \tag{2.4}$$

and CO_2 photolysis:

$$CO_2 + h\nu \rightarrow CO + O. \tag{2.5}$$

Among these two processes, CO_2 photolysis is the dominant one (Minschwaner et al., 2010) and becomes increasingly important with height in the upper mesosphere and lower thermosphere due to incoming solar radiation in the Schumann-Runge continuum and Lyman-α wavelength. Because of this increase in CO_2 photolysis with altitude, the CO distribution is characterised by a large vertical concentration gradient, as can be seen in Figure 2.1a, showing a global average of mesospheric CO concentration profiles from all the SMR CO observations. The photochemical lifetime of CO is greater or equal to the zonal, meridional and vertical transport time scales in the middle atmosphere, ranging from a few days in the stratosphere to several hundreds of years at 100 km altitude (Brasseur et al., 2005). Because of this, and due to its large vertical concentration gradient, CO is suitable for use as a tracer of dynamics in this region (Lee et al., 2011; Zafra et al., 2004) (see Section 3).

2.2 H_2O chemistry

H_2O is a very important species for the middle atmosphere for different reasons. In the lower stratosphere, H_2O is the most important greenhouse gas. Thus, an increase in humidity at this altitude can impact global warming at surface level. Moreover, H_2O is involved in ozone depletion because it is a component of polar stratospheric clouds on which surfaces take place reactions which lead to ozone depletion. H_2O is also a main source of hydrogen radicals (such as OH, H, HO_2) which destroy ozone through catalytic reactions, especially in the lower stratosphere. In addition to that, H_2O is, like CO, a useful tracer of mesospheric circulation, due to its long photochemical lifetime which is of the order of months at the stratopause and of a few days at 100 km (Brasseur et al., 2005). Major sources of H_2O in the stratosphere are the uplift of moist air from the troposphere through the tropical tropopause, and the convective upwards transportation of ice particles which then evaporate and cause increase in water vapour in the stratosphere. Tropospheric H_2O can also reach the stratosphere along isentropic surfaces that cross both layers or be injected by volcanic eruptions (Lossow et al., 2019). A source of H_2O in the middle atmosphere is methane oxidation:

$$CH_4 + 2 \cdot O_2 \rightarrow 2 \cdot H_2O + CO_2. \tag{2.6}$$

This process is more important in the stratosphere than in the mesosphere, since it decreases with height due to smaller abundances of CH_4, becoming negligible between 60 - 70 km. Above those altitudes, H_2 oxidation becomes the dominant source through the reactions:

$$H_2 + O \rightarrow H_2O \tag{2.7}$$

$$H_2 + O_3 \rightarrow H_2O + O_2. \tag{2.8}$$

Photodissiociation is the only major sink of H_2O in the mesosphere. It takes place via the following reactions:

$$H_2O + h\nu \rightarrow H + OH \quad (\lambda < 200 \text{ nm}) \tag{2.9}$$

and

$$H_2O + h\nu \rightarrow H_2 + O(^1D) \quad (\lambda < 170 \text{ nm}). \tag{2.10}$$

A minor sink, limited to the lower mesosphere and negligible compared to the photodissociation effects, is reaction with $O(^1D)$:

$$H_2O + O(^1D) \rightarrow 2 \cdot OH. \tag{2.11}$$

Due to increasing ultraviolet flux, photodissiociation becomes more important with altitude and dominates above 70 km, causing H_2O concentration to decrease with altitude (as can be noted in Figure 2.1b) (Nicolet, 1984; Lossow et al., 2019).

2.3 NO chemistry

NO plays an important role in the middle atmosphere for various reasons. Its concentration is strongly affected by variations in solar and geomagnetic activities (see below and Chapter 4), therefore NO is an indicator of energy input in the middle atmosphere. It also contributes to cooling of the lower thermosphere via infrared emission (Mlynczak et al., 2003). Moreover, NO and more generally nitric oxides (NO_x), i.e. NO and NO_2 altogether, are involved in the ozone (O_3) catalytic destruction and its consequent depletion in the stratosphere. In particular, the NO_x catalytic cycle is the main O_3 destruction cycle between about 25 and 40 km (Crutzen et al., 1975). This happens via the following reactions:

$$NO + O_3 \rightarrow NO_2 + O_2 \tag{2.12}$$

$$NO_2 + O \rightarrow NO + O_2. \tag{2.13}$$

Reaction 2.12 and NO_2 photodissociation

$$NO_2 + h\nu \rightarrow NO + O(^3P) \quad (\lambda < 405\text{nm}) \tag{2.14}$$

are in equilibrium in the sunlit middle atmosphere, and the NO/NO_2 ratio is ≈ 1 up to 40 km altitude. Above this level, the ratio grows rapidly with altitude, through Reaction 2.13, due to increasing atomic oxygen density. During nighttime, Reaction

2.12 is not contrasted by NO_2 photodissociation and this causes the rapid conversion of NO into NO_2 up to about 60 km. Above this altitude, O_3 concentration becomes very low and NO can be considered as a proxy for NO_x.

In the stratosphere, NO is mainly produced from oxidation of N_2O originating in the troposphere (e.g., McElroy et al., 1971):

$$O(^1D) + N_2O \rightarrow 2 \cdot NO \tag{2.15}$$

where $O(^1D)$ is excited oxygen which is produced from ozone photolysis (Crutzen et al., 1975):

$$O_3 + h\nu \rightarrow O(^1D) + O_2 \quad (\lambda < 310 \text{ nm}). \tag{2.16}$$

This production is more intense at low latitudes due to tropospheric dynamics resulting in a stronger uplift of N_2O at the equator, where NO production reaches a peak of 100 molec $\cdot$ cm^{-3} $\cdot$ s^{-1} (Crutzen et al., 1983).

In the mesosphere and lower thermosphere (MLT), the main source of NO comes from the reaction between excited nitrogen ($N(^2D)$) and molecular oxygen:

$$N(^2D) + O_2 \rightarrow NO + O, \tag{2.17}$$

while the same reaction takes place much more slowly when ground state nitrogen ($N(^4S)$) is involved (Brasseur et al., 2005). Excited nitrogen is formed by several different processes at different latitudes. At high latitudes, $N(^2D)$ is formed due to precipitation of energetic auroral and radiation belt electrons (see Section 4.3), with energies larger than 10 keV:

$$N_2 + e^* \rightarrow N(^2D) + N(^4S) + e^*. \tag{2.18}$$

EPP - which will be described in more details in Chapter 4 - is therefore the dominant source of NO in the MLT at high latitudes (Sinnhuber et al., 2012). At low latitudes instead, energetic electrons for Reaction 2.18 are produced by photoionization of gases by solar soft X-rays (Marsh et al., 2004).

Another source of excited nitrogen in the MLT is the dissociative recombination of N_2^+:

$$N_2^+ + e \rightarrow N(^2D) + N(^4S), \tag{2.19}$$

where N_2^+ is a product of molecular nitrogen ionization by auroral and radiation belt electrons - in the lower thermosphere and mesosphere, respectively - and solar protons - mostly in the stratosphere (see Sections 4.2 and 4.3) (Sinnhuber et al., 2012).

Excited nitrogen in the MLT is also produced by dissociative recombination of ionised nitric oxide:

$$NO^+ + e \rightarrow N(^2D) + O, \tag{2.20}$$

with NO^+ being produced via ultraviolet photons ($\lambda < 137$nm) with energies above 9 eV (Sinnhuber et al., 2012).

Since both energetic electrons (see Chapter 4) and UV fluxes increase with altitude in this part of the atmosphere, NO concentration increases with height (Siskind et al., 1998), as shown in Figure 2.1c.

Loss of NO in the MLT occurs during daytime due to photodissociation by solar UV radiation:

$$NO + h\nu \rightarrow N(^4S) + O \quad (\lambda < 190.8 \text{ nm}) \tag{2.21}$$

which in turn leads to the formation of ground state nitrogen ($N(^4S)$), also responsible of NO depletion:

$$N(^4S) + NO \rightarrow N_2 + O. \tag{2.22}$$

Consequently, the photochemical lifetime of NO, which is less than one day in the sunlit MLT, can extend to several weeks during polar night when no photochemical loss occurs (e.g., Randall et al., 2007), making NO also a useful tracer of middle atmospheric circulation under such conditions.

From Reactions 2.17, 2.18, 2.19 and 2.22 it is clear how NO concentration depends on the ratio between excited and ground state atomic nitrogen, on which there are large uncertainties. For example, an increase in the $N(^2D)/N(^4S)$ ratio from 0.5 to 0.6 would result in an 80% increase of NO concentration (Barth, 1992). In general, large uncertainties in the reaction rates of some of the above described reactions still exist today. It is hard to perform laboratory measurements under conditions representative of the MLT (Sinnhuber et al., 2012). Observations are therefore needed to solve such uncertainties.

Chapter 3

Middle atmospheric dynamics

Middle atmospheric dynamics is driven by heat differences and by momentum deposition by breaking waves. The former are responsible for the formation of zonal winds, the latter is required for the establishment of meridional flows. In Figure 1.1 the zonal flows are represented by the white circles, with letters W and E representing westerlies and easterlies respectively. Except for regions affected by strong wave forcing, zonal winds at these altitudes consist of geostrophic winds, i.e. winds that result from the balance between the Coriolis force and the pressure gradient force. Therefore, the vertical gradient of the zonal wind is proportional to the meridional temperature gradient via the thermal wind relation:

$$f \cdot \frac{\partial u}{\partial z} = -\frac{R_{air}}{r_{Earth} \cdot H} \cdot \frac{\partial T}{\partial \phi} \tag{3.1}$$

where f is the Coriolis parameter (positive in the northern hemisphere, negative in the southern hemisphere), u the zonal wind, z the altitude, R_{air} the gas constant for air, r_{Earth} the radius of the Earth, H the scale height and ϕ the latitude (Brasseur et al., 2005). If there is an increase or decrease of zonal winds in intensity with altitude, or if easterlies (negative u) take place rather than westerlies (positive u), this is determined by the signs of f and the meridional temperature gradient.

3.1 Large-scale circulation

Atmospheric waves consist of periodic perturbations of atmospheric variables (temperature, pressure, etc.). Waves which are generated at low altitudes propagate upwards and, because of decreasing air density grow and eventually become unstable and dissipate. The meridional circulation in the middle atmosphere is driven by momentum deposition of breaking waves of two types: planetary-scale Rossby waves and smaller scale gravity waves. Simply stated, the former drive the circulation in the stratosphere, the latter drive it in the mesosphere. Rossby waves (whose direction of propagation is represented by solid red lines in Figure 1.1) are generated in the troposphere due to thermal forcing associated with sea/land contrast, or due to the encountering of obstacles - such as mountains - by air flows. Their wavelengths range

from 5000 to 20000 km and they can be either stationary or travel longitudinally with periods ranging from a few days to a few weeks. These waves have the Coriolis force as restoring force and are mainly generated in the northern hemisphere, since it is characterized by more landmass than the southern hemisphere. They dissipate in the stratosphere exerting a negative drag that, in northern winter, is responsible for deceleration of the westerlies and, consequently, for the forcing of a poleward flow. Because of mass conservation, the poleward flow causes upwelling in the tropics and downwelling at the extra-tropics, resulting in the so-called Brewer-Dobson circulation (represented by the black arrows in correspondence of the stratosphere in Figure 1.1) (Brewer, 1949). Since Rossby waves are mostly generated in the northern hemisphere, the Brewer-Dobson circulation is more intense in the northern than in the southern hemisphere.

Other waves that drive the meridional circulation are gravity waves (direction of propagation represented by the dashed red lines in Figure 1.1) which are characterised by significantly shorter wavelengths than Rossby waves (typically 10 to 1000 km) and have buoyancy as restoring force (Shepherd, 2000). They form when parcels in a stably stratified fluid are displaced vertically and the return to the position of equilibrium gives rise to oscillations. Displacement of parcels occurs due to different mechanisms such as convection, wave-wave interaction, frontal systems and irregular topography. Gravity waves propagate up to the mesosphere where they dissipate. While propagating, they undergo filtering determined by the zonal velocity of the winds encountered on the path. More specifically, a gravity wave is absorbed when its zonal phase velocity equals the zonal velocity of the background wind; therefore only gravity waves with a zonal phase velocity greater than - or opposite to - the mean zonal wind velocity can propagate upward. These waves then break in the mesosphere, driving the air motion out of geostrophic balance. Thus, when breaking in the winter hemisphere, they cause a negative drag that weakens the westerlies, forcing a equator-to-pole flow; while in the summer hemisphere they cause a positive drag, weakening the easterlies and forcing a pole-to-equator flow. The combination of these two flows results in a pole-to-pole flow, from the summer hemisphere to the winter hemisphere, and in an associated upwelling at the summer pole as well as a downwelling at the winter pole (see black arrows in correspondence of the mesosphere in Figure 1.1). The upwelling and the downwelling cause, respectively, an adiabatic cooling at the summer pole and an adiabatic heating at the winter pole, thus resulting in mesopause temperatures being lower above the summer pole (as mentioned in Chapter 1), despite the higher exposure to solar radiation.

At the poles, during local winter, a polar vortex also forms, causing a descent of cool air from the upper mesosphere to the lower stratosphere. The polar vortex consists of a low-pressure region - with an area between 2 and 3 $\cdot 10^7$ km^2 at $\sim$20 km altitude and around 1.5 $\cdot 10^7$km^2 at $\sim$70 km (Schoeberl et al., 2003) - that rotates counter-clockwise at the north pole and clockwise at the south pole. Due to its dependence on temperature difference between the tropics and the poles, it occurs only during local winter, giving rise to a strong meridional temperature gradient

across its front. The front separates an area of cold dry air inside the vortex from an area of warm moist air outside of it. These winter polar downward currents result in the descent of CO- and NO-richer air coming from higher altitudes. The downwelling winter air is also dryer, resulting in lower H_2O concentrations to be observed at the poles during local winter (see Figure 3.1). On the other hand, in the summer polar region, the upwelling causes water vapour to reach the mesopause, resulting in an increase of H_2O concentration (Lossow et al., 2019).

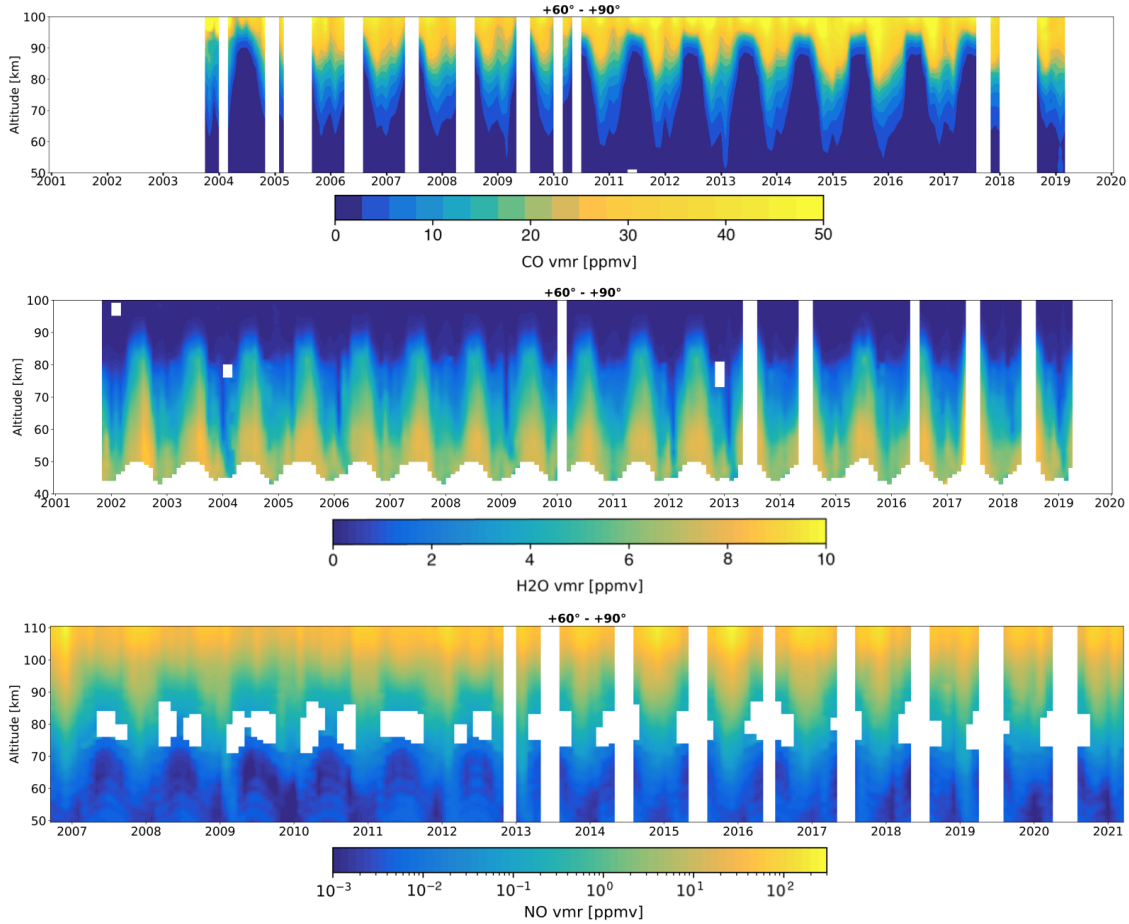

Figure 3.1: Time series of CO (top), H_2O (middle) and NO (bottom) volume mixing ratios measured by SMR for the $+60° - +90°$ latitude band, taken from Paper 1, 2 and 3 respectively. The white bands indicate months during which the number of scans in the given latitude band is lower than 10. The ticks on the x-axis correspond to the beginning of each year. Note the different colour scales and axes.

During some winters, the polar vortex is disturbed by planetary waves propagating upwards from the troposphere (e.g. Charlton et al., 2007). For this reason, the descent of cold air gets disrupted and temperatures several tens of Kelvins higher than usual are registered at high latitudes in the stratosphere. These increase in temperature occurs within a few days, therefore these phenomena are known as Sudden Stratospheric Warmings (SSWs). Since planetary waves originate mostly in the northern hemisphere, SSWs take place almost exclusively in the northern polar

region. Only two events have been recorded in the Southern hemisphere under the last 20 years, while this happens very regularly in the North. After such an event, the vortex recovers and, in some cases, the descent restarts from higher altitudes than usual (Orsolini et al., 2017) causing drier and more CO- and NO-rich air to be transported downwards. These changes in concentrations can be observed in Figure 3.1, in particular during later part of winters 2008-09, 2012-13 and 2018-19. In such cases, the stratopause reforms at altitudes 10 to 20 km higher than usual (Vignon et al., 2015) (we then talk about SSWs followed by an elevated stratopause, SSW-ES).

Gravity waves are also responsible of the presence of Semi-Annual Oscillation (SAO) of zonal winds in the tropics (Ray et al., 1998). The easterly phase of stratospheric SAO of zonal winds is driven by meridional advection of easterlies from the summer hemisphere across the equator, together with the breaking of Rossby waves. The westerly phase instead is driven by momentum deposition of gravity waves. Furthermore the mesospheric SAO is driven by gravity waves generated in the troposphere and propagating towards higher altitudes. While travelling through the stratosphere, these waves are filtered by the local zonal wind SAO so only gravity waves with opposite zonal phase velocity reach the mesosphere and break there. This wave filtering does so that mesospheric SAO has a phase shift of 180° compared to stratospheric SAO. The SAO of zonal winds leads to a SAO in meridional circulation and, consequently, in mean vertical motion as well. In Figure 3.2 it can be noticed how mean vertical motion SAO has an effect on mesospheric CO, NO and H_2O concentrations above the tropics. In particular, sinking or weak rising motion of air causes the presence of higher CO, higher NO and lower H_2O concentrations in correspondence with the equinoxes. Viceversa, solstices are characterised by a stronger rising motion, therefore lower CO, lower NO and higher H_2O concentrations are observed.

3.2 Atmospheric tides

Another important dynamical process affecting the whole atmosphere is atmospheric tides. They are planetary-scale oscillations in various atmospheric fields, that is wind, temperature, pressure, density and geopotential height, among others. This section presents a summary of their main characteristics in the middle atmosphere (see Oberheide et al. (2015) for more information).

Atmospheric tides can be of solar or lunar origin: the former ones can be excited by the absorption of solar radiation, by large-scale latent heat release in the tropics connected to convective clouds in the troposphere, by the gravitational pull of the Sun, or by non linear wave-wave interactions; the latter ones are forced by the Moon's gravitational pull. In all cases the restoring force of the tides is gravity. Tidal oscillations have periods which are an integer fraction of a solar (24 h) or lunar (24.8 h) day, according to their origin. Solar atmospheric tides are the dominating ones, with temperatures and wind speeds that can vary by more than 60 K and 100 m/s in the lower thermosphere, whereas lunar tides are only 5-10% as large and

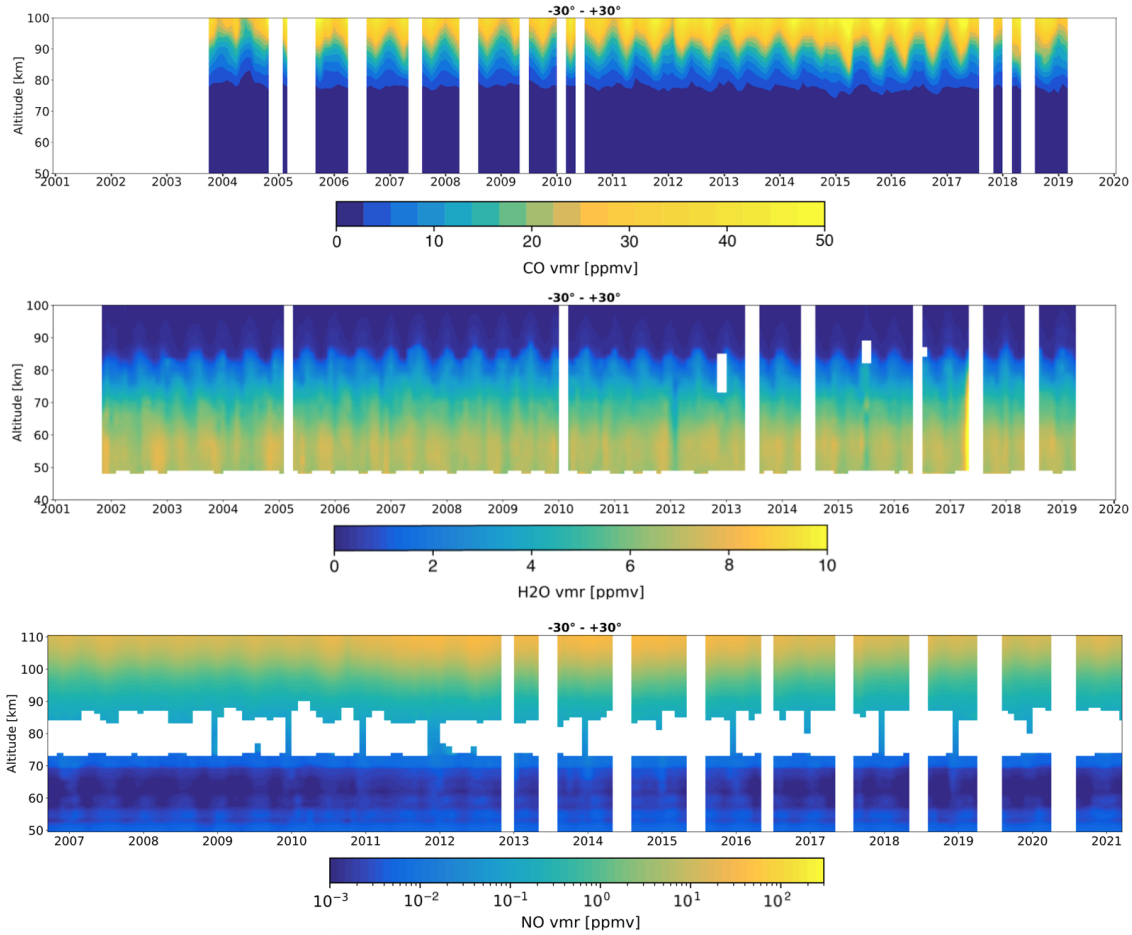

Figure 3.2: Time series of CO (top), H_2O (middle) and NO (bottom) volume mixing ratios measured by SMR for the -30° – +30° latitude band. Figures in the top and middle panels are taken from Paper 1 and 2 respectively, while the figure in the bottom is representative of the NO data set used in Paper 4. The white bands indicate months during which the number of scans in the given latitude band is lower than 10. The ticks on the x-axis correspond to the beginning of each year. Note the different colour scales and axes.

can cause variations in the wind speed of around 10 m/s at such altitudes. The main lunar tide has a semidiurnal period and it is directly due to the gravitational pull of the Moon on the Earth's atmosphere which is maximum at low latitudes, while other minor lunar atmospheric tides are indirectly forced by the gravity through ocean tides. As mentioned above, solar atmospheric tides cause significantly larger oscillations in atmospheric fields than lunar tides. Various components of such tides are strong enough to be observed and have been subject of studies. These components are usually identified by a series of letters and numbers which give information about the frequency (e.g. D for diurnal and S for semidiurnal), propagation direction (E for eastward, W for westward) and zonal wave number. Solar atmospheric tides are usually divided into two types: migrating and nonmigrating tides. Migrating tides propagate westward, following the apparent motion of the Sun, and originate from the absorption of solar radiation by the atmosphere. In particular, progressively longer

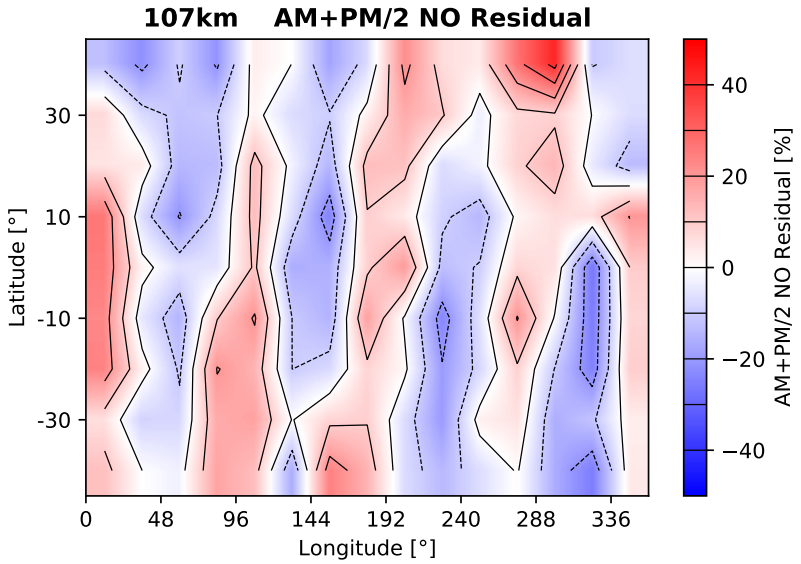

Figure 3.3: December monthly climatology of lower thermospheric SMR average pairs of ascending and descending NO measurements, taken between -40° – + 40° latitude at 107 km altitude. The colors represent the deviation in percentage from the zonal mean, also known as residual. The effect of a semidiurnal solar nonmigrating tide on NO mixing ratio is visible in the 4-wave like structure. From Paper 4.

wavelengths are absorbed as solar radiation reaches lower altitudes, and therefore different tides originate at different altitudes: at 100-150 km altitude molecular oxygen (O_2) absorbs far-ultraviolet radiation (100-200 nm), at 30-70 km ozone (O_3) absorbs near-ultraviolet radiation (200-300 nm), and water vapour (H_2O) absorbs infrared radiation in the troposphere. The upward propagating components of the waves grow in amplitude as they propagate towards higher altitudes where the density is lower, due to conservation of energy. For this reason, even though no solar tides originate in the upper mesosphere (80 - 100 km), this region is affected by strong tidal oscillations (with tidal winds being larger than mean winds) originating at lower altitudes and propagating upwards. The upper mesosphere shows the presence of mainly two components of migrating solar tides: a diurnal one (DW1) originating in the troposphere (from absorption of solar infrared radiation) and a semidiurnal one (SW2) (from near ultraviolet absorption). Since the diurnal tide originates at lower altitudes, it grows over a deeper altitude region compared to the semidiurnal component. Therefore, once it reaches the upper mesosphere, DW1 amplitudes are approximately two times larger than SW2 amplitudes in the same altitude region.

On the other hand, nonmigrating tides are not Sun-syncronous, so they either propagate eastward or they propagate westward more rapidly or more slowly than the projection of the Sun. A source of nonmigrating tides (such as DE3, DE2 and SE2) in the troposphere is latent heat release connected to convective clouds, which is particularly important at low latitudes where there is more evaporation due to a greatest absorption of solar radiation. Nonmigrating tides can also be generated by the interaction between planetary waves and migrating tides (examples are DW2

and D0, where number 0 indicates a standing wave). An example of nonmigrating solar tide can be observed in Figure 3.3.

Chapter 4

Energetic particle precipitation's impact on the middle atmosphere

4.1 Energetic particles

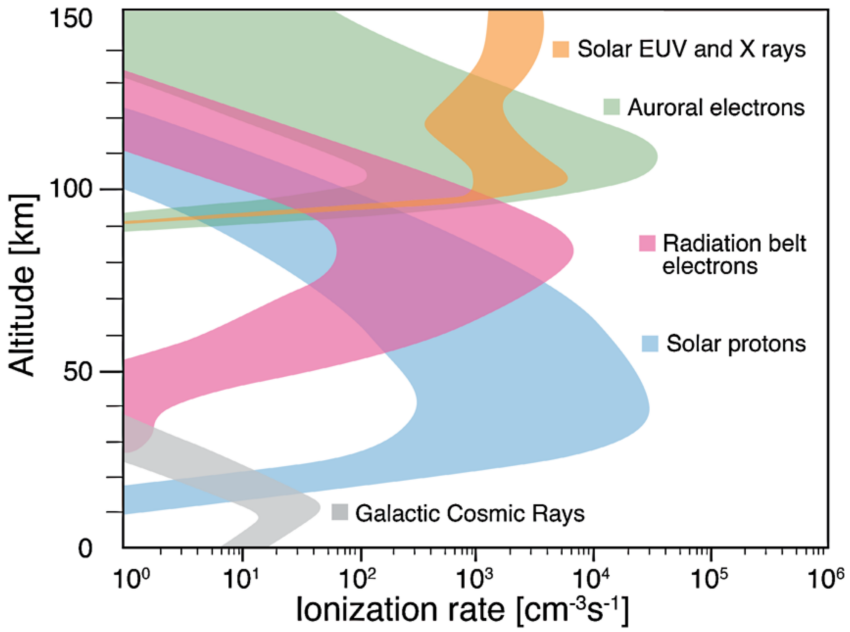

Figure 4.1: Ionization rates of solar EUV, X-rays, auroral electrons, radiation belt electrons, solar protons and galactic cosmic rays in the atmosphere. From Mironova et al. (2015).

When considering the impact of solar activity on climate, IPCC reports currently take into account only variations in solar irradiance (Masson-Delmotte et al., 2021). However, it has been observed that also energetic particle precipitation (EPP) can have an impact on Earth's atmospheric chemistry and dynamics, although uncertainties on measurements still don't allow the accurate quantification of the magnitude of some of these effects (Sinnhuber et al., 2012). Energetic Particles (EPs)

originate mostly from outer space and precipitate into the atmosphere where they are responsible for the ionization of various species and thus affect the composition of the atmosphere. They are the most important source of ionization below 100 km, where most solar energetic ultraviolet (EUV) radiation and X-rays do not penetrate due to their absorption at higher altitudes (Figure 4.1). EPs also cause ionization above 100 km, where auroral low-energy electrons and protons (with energy less than 30 keV and 1 MeV respectively) collide with ionospheric molecules and atoms. On the other hand, the EPs with the highest energy are Galactic Cosmic Rays (GCRs) from outside the solar system, with energies from around 10^7 up to around 10^{21} eV, which can penetrate down to altitudes below 40 km. They consist of ∼90% protons, ∼10% He nuclei and ∼1% other nuclei. Electrons are also a minor component, amounting to about 1% of GCRs. However, the EPs that are mostly responsible for ionization in the middle atmosphere are solar protons and radiation belt electrons (Mironova et al., 2015), as it will be explained in Sections 4.2 and 4.3. Furthermore, in Section 4.3, it will be described how also auroral electrons have an indirect impact on the middle atmosphere, despite causing ionization mainly at higher altitudes.

4.2 EPP Direct Effect

Charged particles originating from the sun usually don't have enough energy to penetrate Earth's magnetic field. However, during periods of high solar activity, coronal mass ejections from the sun sporadically accelerate charged particles to energies that, at geostationary orbit altitudes (i.e. around 36000 km), have been measured to be between 1 MeV and several GeV. These solar energetic particles (SEPs) are then deviated by the Earth's magnetic field towards the poles and the more energetic they are the deeper in the atmosphere they can penetrate (Sinnhuber et al., 2012). The composition of SEPs is dominated by protons which amount to more than 90% of the total (Miroshnichenko et al., 2008), therefore we refer to these sporadic increases in SEPs flux as solar proton events (SPEs). The flux enhancement corresponding to an SPE can last for several days in the case of particles with energy between 100 MeV and several GeV, whereas it can last for several weeks or months for particles with energy below 100 MeV (Bazilevskaya, 2005). SEPs with energies below 100 MeV are the most abundant. These cause ionization in the upper polar stratosphere and in the mesosphere, that is between 40 and 90 km altitude. Particles with energies above 100 MeV instead penetrate down to lower stratospheric altitudes (around 10 km) (Velinov et al., 2013). The ionization caused by SPEs leads to the production of NO_x species in the mesosphere and stratosphere, where they react with O_3 and cause its depletion (Funke et al., 2011) (see Reactions 2.12 and 2.13 in Section 2.3). The process by which O_3 is depleted at the same altitudes where NO_x are produced by SPEs, is known as EPP direct effect (EPP-DE). It has been observed that SPEs can cause the depletion of stratospheric O_3 by more than 10% for up to 5 months after the event (Funke et al., 2011). EPP-DE can also be caused by medium energy electrons (see Section 4.3) reaching mesospheric altitudes (Sinnhuber et al., 2016).

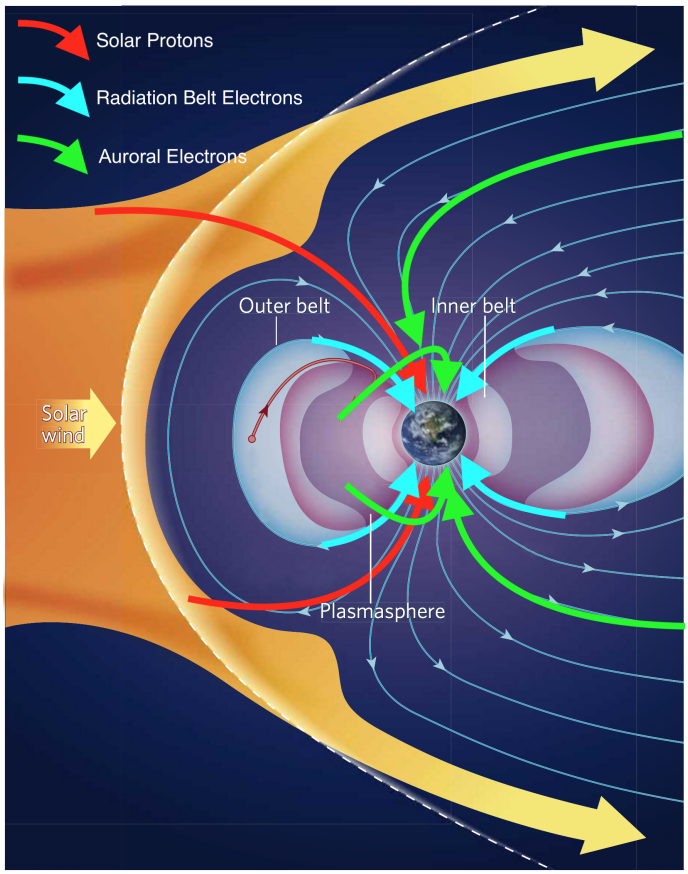

Figure 4.2: Exemplary trajectories of precipitating solar protons (red arrow), radiation belt electrons (light blue arrow) and auroral electrons (green arrow). Van Allen radiation belts are represented by the light blue areas and the plasmasphere by the purple ones. The magnetotail is only partially shown here, in its part nearest to Earth, represented by the magnetic field lines in the right side of the figure. Edited from Rodger et al. (2008).

4.3 EPP Indirect Effect

The flow of charged particles originating from the solar upper atmosphere - called solar wind - creates disturbances in the Earth's magnetic field, and these disturbances are particularly intense in correspondence of solar flares and coronal mass ejections, when strong geomagnetic storms are triggered. One of the consequences of such events is that charged particles from the Earth's plasmasphere and magnetotail are deviated towards the poles and precipitate down to the thermosphere (e.g., Schroeder et al., 2021). The plasmasphere is a toroidal region of low energy charged particles, extended between 1000 km and 28000 altitude (or up to 51000 km during periods of low geomagnetic activity), rotating along with the Earth; while the magnetotail is the part of the Earth's magnetosphere facing away from the Sun and extending as far as 300000 km from the Earth's surface. The magnetotail also encloses low energy charged particles (e.g., Parks, 2015). Both the plasmasphere and the magnetotail are shown in Figure 4.2. Protons and electrons from these regions reach the thermosphere with energies below 30 keV and 1 MeV respectively (Mironova et al., 2015), causing

ionization and excitation of atmospheric constituents in the thermosphere (mostly N_2 and O_2), and giving rise to auroras lights resulting from various species de-excitation. Hereafter, we will refer to such charged particles as auroral protons and electrons. The precipitation of auroral electrons, in particular, is the major driver for ionization in the thermosphere (e.g., Galand et al., 2002), with maximum ionization rates reached in the lower thermosphere (see Figure 4.1), and leads to the production of NO_x and HO_x (OH, HO_2, H_2O_2) species (Mironova et al., 2015).

Electrons and protons from the solar wind - together with trace amounts of He and other heavier nuclei - can also be trapped by the Earth's magnetic field inside the so called Van Allen radiation belts. They consist of two main belts, partly overlapping with the plasmasphere: an inner one located between 1000 - 12000 km altitude and dominated by protons (with energies above 100 MeV), and an outer one located between 13000 - 60000 km altitude containing mostly electrons (with energies between 0.1 – 10 MeV) (Ganushkina et al., 2011). Therefore the energy of the charged particles in the Van Allen belts is considerably higher than those to be found in the rest of the plasmasphere and in the magnetotail. The stable motion of particles in the radiation belts around the Earth can be broken due to very low frequency (VLF) signals generated by magnetic storms, lightning, earthquakes, or anthropogenic VLF signals. Interactions between such signals and the particles in the radiation belts can cause pitch-angle scattering and loss of energy of the latter and their consequent precipitation. Since the outer belt is more affected by solar activity, it is mainly electrons in this belt which are subject to precipitation (Clilverd et al., 2010). This is represented in Figure 4.2. The energy spectrum of the precipitating electrons can vary from one event to another as the VLF signals which trigger the precipitations can have different origins and energies. The radiation belt electrons which precipitate towards the poles are mostly medium energy electrons, with energies between 30-300 keV. They usually don't penetrate below 50 km altitude due to energy losses through radiation and ionization (Mironova et al., 2015). The ionization rate caused by their precipitation towards the poles is maximum in the mesosphere (see Figure 4.1), leading to the production of NO_x and HO_x species.

The reactions that involve low and medium energy electrons in the production of NO_x are presented in Section 2.3. Thus produced thermospheric and mesospheric NO_x, during polar winter, are transported down to the lower mesosphere and stratosphere by the downward branch of the middle atmospheric residual circulation (see Section 3), and here they react with O_3, causing its catalytic destruction. This doesn't apply to HO_x which have a much shorter lifetime than NO_x, therefore the response of an increase in HO_x concentration is very localised, both in time and in space. Regarding NO, the downward transport is possible because, in polar night conditions, it can have a lifetime of several weeks, while it is rapidly photodissociated in the sunlit mesosphere (see Section 2.3) (Funke et al., 2005). In particular, during SSW-ES winters (see Section 3.1), after the reformation of the polar vortex, stronger descents occur from higher altitudes than usual, resulting in higher NO_x concentrations to be observed in the lower mesosphere and stratosphere (Funke et al.,

2014; Pérot et al., 2021). The transport of these species produced by EPP at higher altitudes, down to heights where they can contribute to ozone depletion, is called EPP indirect effect (EPP-IE). This phenomenon has been studied in Paper 3, where the EPP-NO descending through the polar winter mesosphere has been quantified using Odin/SMR observations of NO. In addition to auroral and radiation belt electrons, also SPEs can produce EPP-IE NO_x, with the corresponding enhancement of NO_x in the lower mesosphere and stratosphere being observed up to several weeks after the event (Randall et al., 2001). It has been shown that in the southern hemisphere, where the polar vortex is usually stable, the interannual variability of EPP-IE is mainly dependent on changes in geomagnetic activity (Randall et al., 2007). This is a consequence of the flux of auroral and radiation belt electrons being affected by geomagnetic activity, as explained above. In the northern hemisphere however, the polar vortex is regularly disturbed by planetary waves, as explained in Chapter 3, affecting in turn the downward transport of NO. The interannual variability in EPP-IE is therefore strongly affected by dynamical activity. In particular, winters affected by a SSW-ES event are characterised by significantly higher fluxes of EPP induced NO (Pérot et al., 2021).

Variations in the geomagnetic activity can be described by several indices. Among these, the Ap index is obtained through measurements of the Earth's magnetic field from 13 different ground observatories located between -44° and +60° latitude. The Ap index is a global daily indicator of the intensity of geomagnetic field disturbances. It is calculated as follows: the daily mean of 3-hourly indices (8 per day) measured at each of the 13 locations is calculated, and then the global mean of these 13 daily local means is calculated. Days with higher levels of geomagnetic activity will present a higher Ap index (Matzka et al., 2021).

Chapter 5

The instrument

Throughout the years it has been possible to improve our understanding of all these dynamical and chemical processes through the development of models and through observations of the atmosphere carried out with various kinds of instruments. Probes on board of balloons and airplanes allow us to carry out in-situ measurements, but to observe different altitudes simultaneously and to have global coverage, remote sensing measurements are needed. Different observation geometries and different techniques are implemented to perform remote sensing of the middle atmosphere. One method consists of using ground-based instruments that look upwards into the atmosphere. One of the advantages with these kind of instruments is that they are easier to maintain, compared to satellite instruments, and are therefore better suited for very long term observations. Moreover, they are suitable for performing measurements above a specific location in a continuous way. The main drawback is that they can cover only one geographical region. Again, to cover larger geographical region, as well as the whole globe, satellite measurements are needed. A summary of the different satellite geometries and techniques that can be used is shown in Figure 5.1. All of them, in contrast with the ground-based instruments, have in common the limitation of not being able to measure local transient phenomena. In addition to that, they cannot be maintained over time in the same way as the ground-based instruments, so they do not provide as long-term observational data sets.

There are two types of observing geometries that satellites can operate with: nadir viewing and limb viewing. The former is used to look straight down to the Earth - to scan around that direction - and mainly perform column integrated measurements. The latter has a line of sight that crosses a longer path through the atmosphere and, by performing measurements at different tangent altitudes, facilitates the estimation of the altitude of the observed molecular species. Vertically resolved observational data can thus be obtained. One way to use limb viewing is to observe direct thermal emission from the molecular species in the middle atmosphere, thus being able to measure throughout the whole orbit, as is the case with Odin/SMR. Limb geometry can also be used to measure limb scattered sunlight with instruments which observe in the UV-visible band. One advantage of thermal emission measurements, in comparison to scattered sunlight ones, is that the former allow us to measure both during daytime and nighttime. Another way of implementing the limb viewing

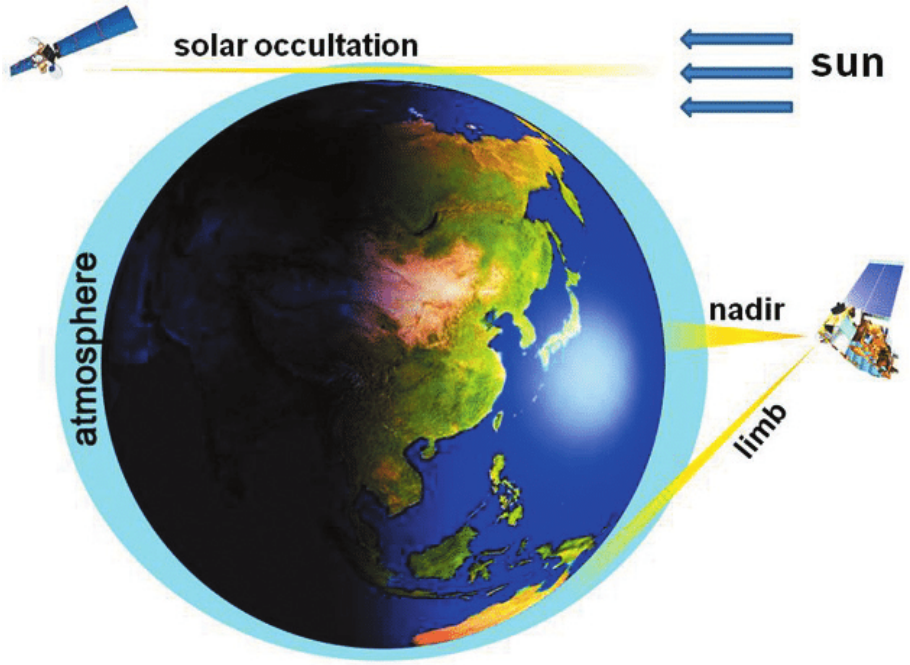

Figure 5.1: Figure summarizing satellite geometries and techniques for atmospheric observations (Lee et al., 2009).

geometry is to use occultation instruments. Solar occultation instruments estimate the concentration of gases in the atmosphere by measuring their absorption of the solar radiation during a sunrise/sunset. There are also stellar occultation instruments that measure various stars instead of the Sun as radiation sources. The advantage of solar occultation instruments is that their measurements present higher signal to noise ratios, and are therefore characterised by better resolution. Since they can perform measurements only during sunrise/sunset, or only when the star used as a source is in the limb view line of sight, occultation instruments perform much fewer measurements than limb sounding instruments measuring thermal emission or scattered sunlight.

5.1 Odin/SMR

The Odin satellite was launched on 20 February 2001 into a circa 600 km sun-synchronous orbit with inclination 97.77° and 18:00 hrs ascending node. The project originated from a collaboration between Sweden, Canada, France and Finland with the purpose of using the satellite for both astronomical and atmospheric observations. Both missions were carried out sharing the observation time until 2007, when the astronomical mission ended. After this date, the observation time has been entirely dedicated to the atmospheric mission. There are two instruments on board Odin: the Sub-Millimetre Radiometer (SMR), on which this thesis is focused, and OSIRIS (Optical Spectrograph and InfraRed Imaging System). Both instruments perform limb sounding of the atmosphere, measuring while scanning in both upwards and downwards directions (see Figure 5.2), with a vertical sampling of ~1.5 km in the

stratosphere to 6 km in the mesosphere depending of the measurement mode. We define a scan as the set of spectra measured between two adjacent turning points. The measured spectrum results from the superimposition of the radiation from all of the emitters enclosed by the beam of the instrument (see Section 5.5) and is assigned a tangent altitude corresponding to the middle of the integration time. The SMR observation schedule features scans that cover different altitude ranges: 7 - 72 km (stratospheric scans), 7 - 110 km (strato-mesospheric scans) and 60 - 110 km (mesospheric scans).

Figure 5.2: Upward and downward scanning of the atmosphere by Odin/SMR.

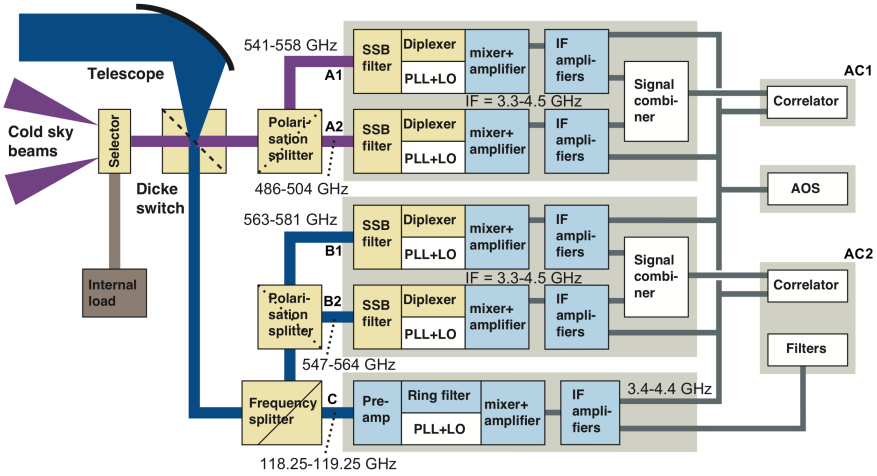

Figure 5.3: Block diagram of the Odin radiometer (Frisk et al., 2003).

A schematic diagram of the major components of SMR is shown in Figure 5.3. SMR has four sub-mm receivers that cover frequencies between 486 - 504 GHz and 541 - 581 GHz allowing us to observe stratospheric and mesospheric O_3, H_2O, CO, NO, ClO, N_2O, HNO_3 emission from rotational transitions. Moreover SMR also presents a mm-wave receiver to detect O_2 emissions at 118 GHz (Frisk et al., 2003). A Dicke switch allows rapid changing of the input source radiation between the main

beam, a hot load and the cold sky, the latter two being used for calibration purposes (Murtagh et al., 2002). The signal travels through a Martin-Puplett interferometer - an interferometer with wire grid polarizer and rooftops mirrors to reflect the signal. In the interferometer, the signal is split into two beams by the polarizer; subsequently, a frequency dependent phase delay

$$\phi(\nu) = 2\pi\frac{2l\nu}{c} \tag{5.1}$$

is introduced between the two components by moving one of the rooftop mirrors and introducing an extra path length (l) in one of the interferometer arms. The response of the interferometer as a function of ϕ is given by:

$$r = \frac{1}{2}[1 + cos(\phi)] \tag{5.2}$$

with maximum and minimum interference occurring respectively when

$$2l = n\frac{c}{\nu} \tag{5.3}$$

and

$$2l = \left(n + \frac{1}{2}\right)\frac{c}{\nu} \tag{5.4}$$

where n is the index of maxima and minima. Therefore, if it is desired to obtain a response of 1 at frequency ν_1 and a response of 0 at ν_0 with no other minima and maxima in between, then the extra path length has to be set to:

$$l = \frac{c}{4|\nu_1 - \nu_0|}. \tag{5.5}$$

In SMR, the extra path length is set so as to suppress the sideband signal resulting from combining the source signal with the one from a local oscillator (LO). The LO is also injected through the Martin-Puplett interferometer. The LO frequency is fine-tuned by means of a Phase-Lock Loop (PLL). This combination of signals is carried out to convert the source frequency from the the 500 GHZ region to a lower one (3.3 - 4.5 GHz). This allows amplification of the signal which would be impossible at the original frequencies, due to technical limitations. The two signals are combined with the use of a Schottky mixer, for which the output signal is a nonlinear function of its input. This implies that the output signal will be a function of the sum and difference of the frequencies of the input signals, therefore consisting of two sidebands: the primary band, including the signal of scientific interest, and the image band. SMR is run in single sideband mode which means that one of the sidebands is suppressed. To avoid the unwanted signal from the image band being included in the measurement, the Martin-Puplett interferometer is used to maximize suppression of those frequencies and maximize transmission of the primary band. However, it is actually not possible to achieve a response of 0, i.e. perfect suppression, and a more correct interferometer response is given by:

$$r = r_0 + \frac{(1-2r_0)}{2}\left[1 + cos\left(\frac{4\pi l\nu}{c}\right)\right] \tag{5.6}$$

where r_0 is the lowest response achieved. Consequently, the sideband leakage will characterize the measurement. It is defined as:

$$p(\nu) = \frac{r(\nu')}{r(\nu) + r(\nu')} \tag{5.7}$$

where ν and ν' are the primary band and image band center frequencies, respectively (Eriksson et al., 2006). Note also a linear dependency of l with respect to the satellite temperature, due to thermal expansion, affecting the response of the interferometer. Eventually, the signal is amplified and directed to the autocorrelator spectrometers.

SMR has two autocorrelator spectrometers (denoted as AC1 and AC2 in Figure 5.3) that filter the input signal into eight sub-bands and calculate the autocorrelation function for each of them. Upper and lower sideband of a same oscillator are used for single-sideband filtering, thus the sub-bands are organised in four pairs of 200 MHz each. The two autocorrelators can be connected to two mixers each (namely AC1 is connected to A1 and A2, and AC2 to B1 and B2) allowing us to measure two 400 MHz blocks simultaneously using one spectrometer. The spectrometers have resolutions that can be set between 150 kHz and 1.2 MHz to which correspond spectral coverages of 100 and 800 MHz respectively (Frisk et al., 2003; Murtagh et al., 2002). To cover different frequencies, the receivers and the spectrometers can be used in different combinations, each one constituting what is called a Frequency Mode (FM).

5.2 Calibration process

The purpose of calibration is to estimate the antenna temperature T_a from the beam signals recorded by the instrument. T_a is defined as the temperature of a hypothetical black body which would result in the same received power at the antenna aperture as in the case of the observed source. Odin/SMR measures three types of beam signals: the cold sky (c_s), the load (c_l) and the main beam signal (c_a). The contributions to such signals for a channel i can be expressed as follows:

$$c_{a,i} = g_i(\eta_a T_{a,i} + T_{rec,i} + (1-\eta_a)T_{amb,i}), \tag{5.8}$$

$$c_{s,i} = g_i(T_{s,i} + T_{rec,i}) \approx g_i T_{rec,i}, \tag{5.9}$$

$$c_{l,i} = g_i(T_{l,i} + T_{rec,i}), \tag{5.10}$$

where g_i is the receiver gain, η_a is the main beam efficiency (assumed to be equal to 1 for sky beam and the load signals), $T_{amb,i}$ is the receiver ambient temperature and $T_{rec,i}$ is the receiver noise temperature. $T_{a,i}$, $T_{s,i}$ and $T_{l,i}$ are the antenna temperature, cosmic background temperature and load temperature, respectively. In Eq. 5.9,

$T_{s,i}$ is negligible in comparison to $T_{rec,i}$ since the former is equal to 0.003 K at 500 GHz and the latter is 3000 K. From the equations above it is possible to derive the unknown $T_{rec,i}$, g_i, η_i and $T_{a,i}$. In particular, g_i and $T_{a,i}$ will be respectively given by (Rydberg et al., 2017):

$$g_i = \frac{c_{l,i} - c_{s,i}}{T_{l,i} - T_{s,i}} \tag{5.11}$$

and

$$T_{a,i} = \frac{1}{\eta_a}\left(\frac{c_{a,i} - c_{s,i}}{g_i} - (1-\eta_a)T_{amb}\right) = \frac{1}{\eta_a}\left((c_{a,i} - c_{s,i})\frac{T_{rec,i}}{c_{s,i}} - (1-\eta_a)T_{amb}\right), \tag{5.12}$$

where the same value of T_{rec} and T_{amb} is used for all spectra within the same scan.

Small perturbations in $T_{s,i}$ and $T_{l,i}$ will result in unwanted features called "ripples" in the calibrated spectra. It can be demonstrated that, when $T_{a,i}$ is approximately 0 K, there is a maximum sensitivity to the perturbations of the cold sky signal (Rydberg et al., 2017). This happens for measurements at high tangent altitudes, where the spectra should be centered around 0 K but instead present a wave pattern. The artifact is removed by fitting median high tangent altitude spectra with a sinusoidal function - whose phase changes with T_{amb} - and removing this wave pattern from the spectra. On the other hand, sensitivity of $T_{a,i}$ to the perturbations in the load signal is minimum when $T_{a,i}$ is close to 0 K and reaches its maximum when $T_{a,i}$ is close to the load temperature, though this never happens. This artifact is hard to detect as it consists of a weak signal in addition to strong atmospheric signal, and is therefore left unresolved.

Another calibration-related artifact arises due to the presence of gain variations which are not captured by the interpolation of the reference signals. So, at a given time t_j during which the main beam is detected, there will be a difference between the estimated ($\hat{c}_s$) and true (c_s) sky beam giving rise to the non-captured gain variation $\Delta g'$:

$$\hat{c}_s(t_j) - c_s(t_j) = \Delta c_s = \Delta g' T_{rec}. \tag{5.13}$$

Note how the gain variation could result in an artifact limited to a sub-band or in a broadband artifact, depending on whether the gain variation originates from a spectrometer or from one of the mixers.

5.3 Technical issues related to CO and H_2O data sets

In Paper 2, causes for artifacts in the SMR H_2O dataset were investigated. In particular, non-linear gain variations were thought to be responsible for the big differences in

H_2O observed with SMR with respect to other instruments. An attempt to quantify such gain variations was made by introducing both a broadband correction factor and a sub-band one, but no value could bring an improvement in the comparison between SMR and other instruments. However, the most probable cause for such discrepancies is thought to be an underestimation of sideband leakages, that is an underestimation of r_0 in Eq. 5.6, for both FMs used for H_2O observations (i.e. FM13 and FM19, both centered around 557 GHz). This underestimation resulted in the fact that spurious signal originating from a sideband leakage was considered as part of the signal of interest, causing a misestimation of retrieved concentration and temperature (see Chapter 6 and Part 2).

Moreover, in Paper 1 it was observed how the malfunctioning of the PLL used for CO observations (performed using FMs 14, 22 and 24, centered around 576.5 GHz) leads to a shift of the LO frequency from its nominal value. This causes a frequency shift in the observed spectra that assumes different values within a same scan. In addition, the PLL malfunctioning has even an effect within the integration time causing line broadening. These issues caused data to be unusable to perform retrievals or lead to a misestimation of the CO concentration (see Chapter 6 and Part 2).

5.4 NO data set

NO is observed by SMR using the FM21 setting, which corresponds to a measured spectral band between 551.15 and 552.15 GHz containing two NO thermal emission lines at 551.45 and 552.05 GHz (Eriksson, 1999). It is measured, both during daytime and nighttime, between 45-50 km and 110-115 km altitude, with a vertical resolution of 3–4 km in the upper stratosphere, 7 km in the mesosphere up to 80 km and of 10 km in the upper mesosphere–lower thermosphere. The latitude coverage of the measurements goes between -82.5° and 82.5°, making SMR the only instrument providing NO observations on a global scale, as of today. Moreover, the SMR NO observations have started in October 2003 and are still continuing. This means that SMR provides one of the longest NO concentration data set available in middle atmosphere. NO observations have been carried out only one day per month before 2007, when the instrument was also used for research in astronomy, whereas the number of measurement days has increased to 4-5 per month after 2007. However, during dedicated observational campaigns, this number can increase significantly (Pérot et al., 2021). Sheese et al. (2013) have shown that systematic errors in the NO measurements amount to 3% from spectroscopic parameters, 2% from calibration and 3%–6% from sideband suppression. The version 3.0 of SMR level 2 NO data is used in Papers 3 and 4. This data set is the result of a recent reprocessing, therefore it has not been subject to a validation study yet. However, Kiviranta et al. (2018) developed an empirical model based on SMR version 3.0 measurements which reproduces NO variability in the mesosphere and lower thermosphere consistently with what was observed by other instruments such as SOFIE (Solar Occultation For Ice Experiment), SCIAMACHY (SCanning Imaging Absorption spectroMeter

for Atmospheric CHartographY), ACE-FTS (Atmospheric Chemistry Experiment - Fourier Transform Spectrometer) and MIPAS (Michelson Interferometer for Passive Atmospheric Sounding).

5.5 Retrieval process

One scan of Odin/SMR L1 data, i.e. the calibrated spectra, can be represented as a vector

$$\mathbf{y} = \begin{bmatrix} \mathbf{y_1} \\ \mathbf{y_2} \\ \vdots \\ \mathbf{y_s} \end{bmatrix}, \tag{5.14}$$

where s is the number of samples in the scan and each element of $\mathbf{y}$ is the spectrum collected at a single tangent altitude, i.e. a brightness temperature value for each frequency bin. An example of a spectrum collected from SMR at 30 km altitude is shown in Figure 5.4. Given the geometry of limb measurements (see the introduction of this Chapter), the spectrum, here featuring CO (left) and O_3 (right) emission lines, is the result of the superimposition of emissions from different altitudes. In Figure 5.5 it can be seen how the shape of the emission contribution varies with altitude, hence the shape of the observed line will be determined by how those variously shaped contributions sum up, i.e. a higher concentration at a certain altitude will cause the corresponding line shape to contribute more to the measured line. Note that the ozone lines shown in the two figures correspond to two different ozone transitions and that the shape of the emission presents a different altitude dependence for different frequency bands. The retrieval process consists in understanding how much a certain line shape, i.e. the emission from a certain altitude, has contributed to the observed line so to obtain concentration and temperature profiles.

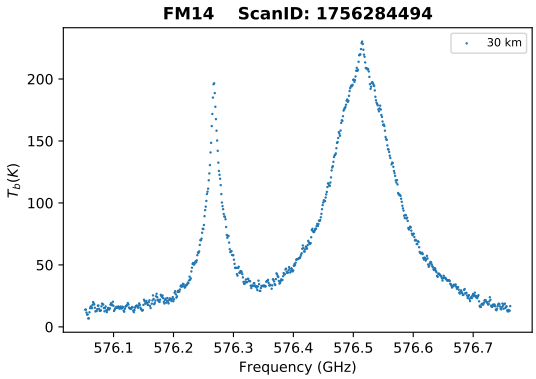

Figure 5.4: 30 km tangent altitude spectrum measured by Odin/SMR featuring CO (left) and O_3 (right) 576 GHz emission lines.

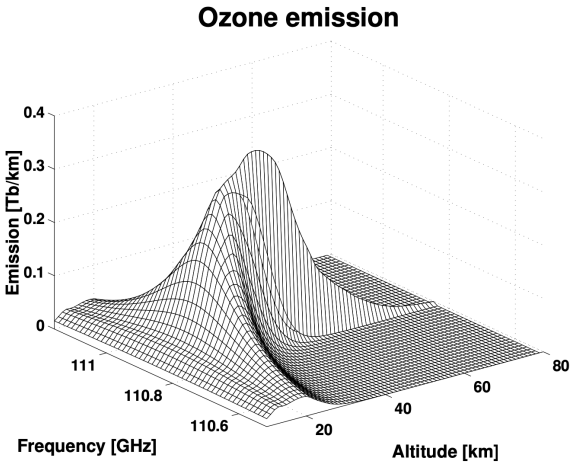

Figure 5.5: Emission from ozone around 110.84 GHz. Note the different line shapes at different altitudes. Figure credit: Patrick Eriksson.

What determines the line shape? Molecular emission lines in the atmosphere are subject mainly to two types of broadening processes: pressure broadening and Doppler broadening. Pressure broadening, resulting in a line shape corresponding to Lorentz profile (Lorentz, 1906), occurs because the higher the pressure of a gas the more frequent the collisions between its molecules will be, resulting in a shortening of the life time of the rotational states involved in the transition. This causes a broadening of the line depending on pressure and temperature according to the following equation:

$$2\gamma_p = 2\gamma_0 \frac{P}{P_0} \left(\frac{T_0}{T}\right)^n \tag{5.15}$$

where $2\gamma_p$, which is the full width at half maximum (FWHM) of the line, has a linear dependence to the pressure P. $2\gamma_0$, P_0 and T_0 are respectively the FWHM, pressure and temperature at the reference level (at the ground level it would be $2\gamma_0 = 3 - 6$ GHz and the index $n = 0.5 - 1$). Doppler shift instead is related to the thermal motion of the molecules. If a molecule emits while in motion toward the observer, this person will observe a line shifted toward higher frequencies; vice versa if the molecule is moving away from the observer. If the gas is in thermal equilibrium then the velocity distribution of the molecules is Gaussian, thus will be also the line shape. Moreover, the higher the temperature of the gas the higher will be the molecules velocity dispersion around the mean velocity, hence the broader the line. The FWHM of the line will be dependent on the temperature T according to the equation:

$$2\gamma_d = 2\frac{\nu_0}{c}\sqrt{\frac{2RT}{M}}, \tag{5.16}$$

where M is the molecular weight in atomic mass and R is the universal gas constant. Pressure broadening dominates at lower altitudes, becoming less and less strong with

increasing altitude (i.e. exponentially decreasing pressure), while Doppler broadening dominates at higher altitudes. As an example, for the ozone line at 500 GHz, pressure broadening dominates until 60 km altitude and Doppler broadening dominates above 80 km. The 60 - 80 km range is characterised by a Voigt line shape, given by a convolution of the pressure and Doppler line shapes. So it is possible, from the observed line, to understand how much a single line shape contributed to the total, therefore deducing concentration and temperature of a species at a certain altitude. For limb sounding, the most important source of altitude information is vertical scanning, though. However, note that Doppler broadening is not dependent on pressure but only on temperature which gives very little information about the altitude, since temperature varies less than pressure with altitude; moreover, Doppler broadening has a low dependence on temperature, i.e. $\sqrt{T}$. So, on the high side, pressure broadening provides information only until a certain altitude; additionally also information about the lowest altitudes is lost, since there the pressure broadening is so big that it causes the line width to be larger than the spectrometer band.

Measurements are performed to retrieve the state vector

$$\mathbf{x} = \begin{bmatrix} \mathbf{v_1} \\ \mathbf{v_2} \\ \mathbf{t} \\ \mathbf{\Delta o} \\ \Delta\theta \\ \Delta\nu \end{bmatrix} \tag{5.17}$$

which consists of $\mathbf{v_1}$ and $\mathbf{v_2}$, i.e. the concentration profiles of the gas species observed using a certain FM, the temperature profile $\mathbf{t}$, the brightness temperature offsets $\mathbf{\Delta o}$ (one for each tangent altitude), the pointing offset $\Delta\theta$ and the frequency off-set $\Delta\nu$. The latter two are scalar values which apply to the whole scan. The three offsets are estimated to compensate inaccurate determination of gain (from calibration), pointing of the instrument (from attitude data) and frequency (from the LO-signal nominal frequency) respectively. If the LO-signal is phase-locked, the frequency offset is assumed to be constant throughout the whole scan. However, if there is a failure in the PLL, like the one that affects the FMs used for CO observations (see Paper 1), then a different frequency correction for each spectrum of the scan is needed.
The inverse problem, i.e. the problem of getting the state vector $\mathbf{x}$ from the measurement vector $\mathbf{y}$ is an ill-posed one, meaning that there are more solutions to it. In fact, several combinations of emission line shapes can sum up to the same observed line. How to know which retrieved state vector is closer to the truth?

First, a forward model ($\mathcal{F}$) with its parameters ($\mathbf{b}$) has to be chosen. Thus the vector $\mathbf{y}$ is related to $\mathbf{x}$ via the following relation:

$$\mathbf{y} = \mathcal{F}(\mathbf{x}, \hat{\mathbf{b}}) + \varepsilon_b + \varepsilon_n, \tag{5.18}$$

where $\hat{\mathbf{b}}$ is the best estimate of the forward model parameters, ε_n is the measurement noise and ε_b is the uncertainty deriving from not knowing the exact values of $\mathbf{b}$. The

forward model used for Odin/SMR retrievals is the Atmospheric Radiative Transfer Simulator (ARTS) (Eriksson et al., 2011) with the assumptions of lack of scattering (valid for SMR sub-mm wavelengths and strato-mesospheric altitudes), local thermal equilibrium and a 1D atmosphere (atmospheric fields only dependent on pressure). The retrieval process can be summarised as follows:

$$\hat{\mathbf{x}} = \mathcal{I}(\mathbf{y}, \mathbf{x_a}, \hat{\mathbf{b}}, \mathbf{c}), \tag{5.19}$$

where $\hat{\mathbf{x}}$ is the retrieved state vector, $\mathcal{I}$ is the inverse model, $\mathbf{c}$ represents the additional variables introduced by the inverse model, and $\mathbf{x_a}$ is an a priori estimate of $\mathbf{x}$, usually coming from a model or from climatology of another instrument.

The approach used here to solve the ill-posed problem (Eriksson, 2015) is the Optimal Estimation Method (OEM), an approach that involves the introduction of a regularisation. To explain what this means, we introduce the cost function:

$$C(\mathbf{x}) = (\mathbf{y} - \mathcal{F}(\mathbf{x}, \hat{\mathbf{b}}))^T \mathbf{S}_o^{-1} (\mathbf{y} - \mathcal{F}(\mathbf{x}, \hat{\mathbf{b}})) + (\mathbf{x} - \mathbf{x}_a)^T \mathbf{S}_a^{-1} (\mathbf{x} - \mathbf{x}_a). \tag{5.20}$$

The OEM consists in minimizing $C(\mathbf{x})$. So the retrieved state vector ($\hat{\mathbf{x}}$) will be given by:

$$\hat{\mathbf{x}} = \min_{\mathbf{x}}(C(\mathbf{x})), \tag{5.21}$$

where $\mathbf{S}_o$ is the covariance matrix of the observation system (i.e. combination of instrument and forward model) and $\mathbf{S}_a$ is the a priori uncertainty covariance matrix. The regularisation is present in the second term of Eq. 5.20 which represents how well the solution agrees with the a priori. If this term weren't present, the obtained $\hat{\mathbf{x}}$ would coincide with the standard least squares solution. So the best solution has to be in accordance with both the measurement and the a priori.

When the retrieval problem cannot be considered linear, i.e. when derivatives of $\mathcal{F}$ and $\mathcal{I}$ are not valid over a significant range, as in this case, an iteration process is needed to determine the solution. The iteration starts by first assuming $\mathbf{x}_a$ as a solution, the successive tentative solution is considered valid if its cost is lower than the previous solution, and so on. The iteration scheme used is the one from the Levenberg-Marquardt method, which involves the use of a parameter γ to evaluate the convergence of the iteration (Rodgers, 2000).

Chapter 6

Summary of appended papers

6.1 Paper 1

Before this study, of the 18 years of Odin/SMR observations of mesospheric CO only data from one year - October 2003 to October 2004 - was usable for scientific purposes. This was the only part of the dataset that was not affected by a malfunctioning of the PLL used for CO observations. The PLL is used to keep the phase of the LO signal stable, and its malfunctioning results in random and continuous modification of the LO frequency. Thus, when LO is combined to the source signal through the mixer, it results in a signal that is also affected by frequency shift. For this reason, most of the CO L1 data were unusable to perform retrievals because the CO line was shifted away from its theoretical position and, in some cases, it was even shifted away from the observed band. These latter extreme cases could not be recovered. For all the other scans, a correction algorithm was developed which allowed to identify the center of the CO line and shift it back to its theoretical position. Not all spectra within a scan were affected by the same shift, therefore a different correction has been applied to each spectrum in the scan. The PLL malfunctioning was affecting the spectra also at a time scale smaller than the integration time, resulting in an artificial broadening of the spectral lines. To take this into account during the retrievals, we have used a broader response function. The CO dataset was thus successfully recovered, providing new mesospheric and lower thermospheric CO concentration profiles which extend between 50 - 100 km and over the whole globe. A validation study has been carried out, comparing SMR observations with the ones from OSO, MIPAS, ACE-FTS and MLS. The overall agreement with the other instruments is very good between 60 and 80 km altitude, with relative differences close to zero. Between 50 - 60 km SMR shows a positive bias up to +20%, while between 80 - 100 km the observed bias is negative and reaching up to -20%. As a result of this study, a new long term data set of CO in the middle atmosphere has been produced. This is very valuable since CO can be used as a tracer of middle atmospheric dynamics.

6.2 Paper 2

Comparisons between H_2O concentrations and temperatures measured by Odin/SMR used to show poor accordance with other instruments. This suggested the presence of an instrumental artifact that was affecting the FMs used for observing H_2O and temperature. Different hypotheses have been investigated. Tests to investigate if the pointing offset of the instrument was too far from the nominal value have resulted negative, as well as tests to look for possible non-linear gain variation which might have caused errors in the calibration. Finally, the most probable cause of SMR H_2O biases have been identified in having underestimated single sideband leakage. Such an underestimation implies that spurious signal from the image band leaking into the primary band is not recognised as such, causing a misestimation of the retrieved concentrations and temperature. A lower value of the minimum suppression, i.e. a greater leakage, have been assumed and new retrievals have been performed, resulting in a new dataset of almost 21 years of H_2O concentration and temperature profiles. The new data are in better accordance with other instruments, compared to the older version. Relative differences in H_2O concentration are always in the $\pm 20\%$ range between 40 - 70 km and diverge at higher altitudes, whereas temperature absolute differences are within ± 5 K between 40–80 km and also diverge at higher altitudes. This study resulted in an improved long-term data set for water vapour in the middle atmosphere, which is particularly valuable, as explained in Section 2.2.

6.3 Paper 3

Significant uncertainties still exist regarding the amount of EPP-IE NO which is transported down to lower altitudes through the mesosphere during polar winters. The purpose of this study was to improve such estimations by analysing Odin/SMR NO mesospheric observations, the only ones from an instrument currently measuring NO globally in the mesosphere, and allowing us to extend the previous data sets further in time. In particular we measured, for 15 years of observations, the total winter flux of EPP-IE NO descending through three isentropic levels in the mesosphere, that is 2600 K, 3300 K and 4000 K. The method used consisted in the following steps: calculating a value for background NO - that is the NO amount already present in the vortex in early winter - as the nighttime in-vortex median of NO concentration during the month prior to the beginning of the winter descent; subtracting this value from the daily median nighttime concentrations inside the vortex; calculating the flux by multiplying the result of the subtraction by the area of the vortex and by the descent rate; integrating the daily fluxes to obtain the total NO flux through the mentioned levels for Northern Hemisphere (NH) winters between 2006-07 and 2020-21 and for Southern Hemisphere (SH) winters between 2007 and 2012. NH winters 2008-09, 2012-13 and 2018-19, affected by SSW-ES events, present the highest NO fluxes at all levels, with measured fluxes between 490 and 1000 Mmol at 4000 K, 310 and 720 Mmol at 3300 K, 270 and 510 Mmol at 2600 K. All other dynamically quiet NH and SH winters present sensibly lower values, which follow a trend similar to variations in geomagnetic activity. The results obtained in this study - which

are consistent with the values presented in similar studies - indicate that dynamics dominate the variability in the total EPP-IE NO fluxes during SSW-ES winters, while the variability during dynamically quiet winters is dominated by geomagnetic activity. Daily and total winter fluxes have been calculated, in both hemispheres, for a high number of winters including the most recent ones which had not been the focus of any study before. These results will be useful to further understand the impact of energetic particle precipitation on the atmosphere.

6.4 Paper 4

In this study, 20 years of lower thermospheric Odin/SMR NO observations at low latitudes were used to estimate how NO mixing ratios in this region are affected by nonmigrating solar tides. SMR, crossing the equator at a different local solar time from other sun-synchronous instruments observing the same atmospheric region, provides unique observations which allowed us to further constraint the amplitude of NO diurnal variations. The focus of this study was on the signatures of nonmigrating semidiurnal tides on NO mixing ratios, whereas previous studies had mainly focused on diurnal tides. For this purpose, monthly climatologies of average pairs of ascending and descending NO observations were calculated. Measurements at 107 km altitude and at latitudes between -40° and +40° were considered, with a focus on -20° latitude. In particular, residuals with respect to the zonal means were calculated, allowing us to study the nonmigrating tidal components and quasi-stationary planetary waves. Subsequently, a Fourier analysis of the spectral components was carried out which indicated how, at -20° latitude, the semidiurnal apparent 4-wave component is dominant throughout all year except in summer, during which the 1-wave component is dominant. Other significant components are the 2- and the 3-wave, both peaking in June. The 4-wave component has a maximum amplitude of 19% in November, whereas the 1-, 2- and 3-wave all peak in June with maximum amplitudes of 19%, 10% and 7%, respectively.

Chapter 7

Thesis contributions and outlook

Odin/SMR has been operating for more than 21 years. It is therefore the most long lived satellite instrument currently performing limb sounding of the middle atmosphere globally. The recovery and improvement of the long term CO and H_2O data sets, presented in Papers 1 and 2, provides valuable measurements of tracers of atmospheric circulation involving all layers of the middle atmosphere. Such measurements can be used for validating models of circulation and chemistry in the middle atmosphere and, given the length of the data sets, can also be used to study long-term trends.

The long photochemical lifetime of NO, under polar night condition, also allows its use as a tracer of middle atmospheric circulation and, in addition to that, enables a coupling of the lower mesosphere and stratosphere to the MLT which occurs through fluxes of EPP-IE NO. These fluxes have been estimated in Paper 3 and can contribute to a better understanding of the impact of energetic particles on the atmosphere.

The study of the mentioned species is useful for the sake of comprehending middle atmospheric processes but also because what happens in the middle atmosphere can have an impact on the troposphere. For example, the EPP-IE contributes to depletion of stratospheric O_3 which in turn can lead to changes in the local thermal structure and dynamics, as well as in the surface climate (e.g., Rozanov et al., 2012; Seppälä et al., 2014); the presence of SSWs can heavily affect the high- and mid-latitude winter weather (e.g., Butler et al., 2017); middle atmospheric variations in H_2O concentration have a significant impact on climate (e.g., Lossow et al., 2019).

Paper 4 focuses on solar atmospheric tides, which are also responsible for coupling of different atmospheric layers, since they generate in one layer and propagate upwards, causing oscillations in concentration and temperature far above the region where they have been generated. The study, in particular, provides estimates of the contribution of different semidiurnal nonmigrating tides to the diurnal variation in NO concentrations in the low-latitude lower thermosphere.

A possible future study utilizing the temperature data sets presented in Paper 2 (see Figure 7.1 for the exemplary $+30° - +60°$ latitude band) is one focusing on the identification of temperature trends in the mesosphere. Models and observations

indeed show that, while the increase in anthropogenic carbon dioxide (CO_2) causes global increase in tropospheric temperature, it also causes a decrease in mesospheric temperatures (e.g., Lin et al., 2019; Bailey et al., 2021). The long term SMR temperature data set would provide a tool to better estimate the rate of this temperature decrease.

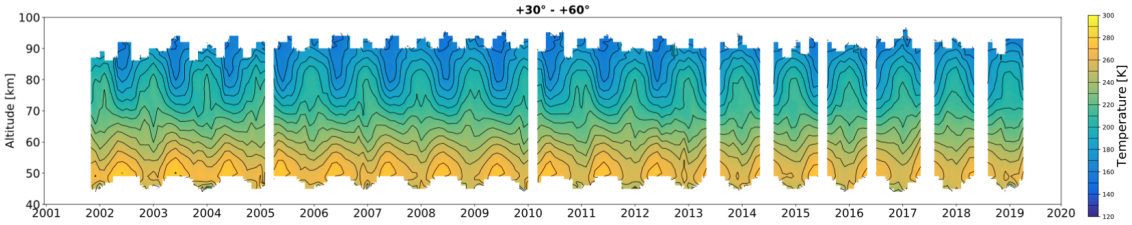

Figure 7.1: Time series of Temperature measured by SMR for the +30° – +60° latitude band, taken from Paper 2. The white bands indicate periods during which the number of scans in the given latitude band is lower than 10. The ticks on the x-axis correspond to the beginning of each year.

The EPP-IE NO fluxes measured in the mesosphere and shown in Figure 7.2 (for northern hemisphere winters) from Paper 3 represent a significant contribution to reducing the existing uncertainties on EPP NO estimation and might thus help to better estimate the natural variability of ozone in future studies. However, these values are probably subject to underestimation due to the assumption that only nighttime measurements are included for the calculation of the medians, and therefore parcels of air that have been exposed to sunlight are not included. However, it can happen that, in early spring, air parcels that were in a sunlit region are then transported in the dark region where the measurement is taken. Some of the NO in these parcels would then be photochemically destroyed before being measured, causing an underestimation of the EPP-IE NO flux value. A further study in which circulation models are used to keep track of such parcels so that they can be removed from the calculation, could significantly improve our EPP-IE estimates. Moreover, the tracking of parcels could also help quantify the amount of NO which leaks out of the polar vortex during the descent. The existence of such leaks is highlighted by the difference in fluxes, during a specific winter, between the different isentropic surfaces, as shown in Figure 7.2. An extension of the study presented in Paper 4, to include also the estimation of the effect of tides on NO concentration at high latitudes, would also help improving the EPP-IE NO flux estimations. In particular, it would allow to better understand how a NO measurement is affected by the local solar time at which it was taken.

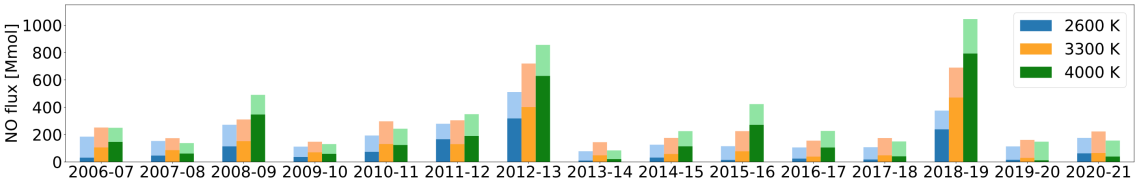

Figure 7.2: Total EPP NO flux calculated in Paper 3, across three isentropic levels 2600 K, 3300 K and 4000 K, based on SMR observations, for all Northern winters considered in the study. Darker colored bars correspond to the median values and lighter colored bars represent the median plus 1σ.

Bibliography

Bailey, Scott M., Brentha Thurairajah, Mark E. Hervig, David E. Siskind, James M. Russell, and Larry L. Gordley (2021). "Trends in the polar summer mesosphere temperature and pressure altitude from satellite observations". In: *Journal of Atmospheric and Solar-Terrestrial Physics* 220, p. 105650. ISSN: 1364-6826. DOI: https://doi.org/10.1016/j.jastp.2021.105650 (cit. on p. 44).

Barth, Charles A. (1992). "Nitric oxide in the lower thermosphere". In: *Planetary and Space Science* 40.2, pp. 315–336. ISSN: 0032-0633. DOI: https://doi.org/10.1016/0032-0633(92)90067-X (cit. on p. 11).

Bazilevskaya, Galina (Dec. 2005). "Solar cosmic rays in the near Earth space and the atmosphere". In: *Advances in Space Research* 35, pp. 458–464. DOI: 10.1016/j.asr.2004.11.019 (cit. on p. 22).

Brasseur, G.P. and S. Solomon (2005). "Aeronomy of the Middle Atmosphere". In: *Springer, The Netherlands, 3rd edition* (cit. on pp. 3, 8, 10, 13).

Brewer, A. W. (1949). "Evidence for a world circulation provided by the measurements of helium and water vapour distribution in the stratosphere". In: *Quarterly Journal of the Royal Meteorological Society* 75.326, pp. 351–363. DOI: 10.1002/qj.49707532603 (cit. on p. 14).

Butler, A. H., J. P. Sjoberg, D. J. Seidel, and K. H. Rosenlof (2017). "A sudden stratospheric warming compendium". In: *Earth System Science Data* 9.1, pp. 63–76. DOI: 10.5194/essd-9-63-2017 (cit. on p. 43).

Charlton, A.J. and L.M. Polvani (2007). "A New Look at Stratospheric Sudden Warmings. Part I: Climatology and Modeling Benchmarks". In: *J. Climate* 20, 449–469. DOI: doi:10.1175/JCLI3996.1 (cit. on p. 15).

Clilverd, Mark A., Craig J. Rodger, Tracy Moffat-Griffin, Emma Spanswick, Paul Breen, Frederick W. Menk, Russell S. Grew, Kanji Hayashi, and Ian R. Mann (2010). "Energetic outer radiation belt electron precipitation during recurrent solar activity". In: *Journal of Geophysical Research: Space Physics* 115.A8. DOI: https://doi.org/10.1029/2009JA015204. eprint: https://agupubs.onlinelibrary.wiley.com/doi/pdf/10.1029/2009JA015204 (cit. on p. 24).

Crutzen, Paul J., Ivar S. A. Isaksen, and George C. Reid (1975). "Solar Proton Events: Stratospheric Sources of Nitric Oxide". In: *Science* 189.4201, pp. 457–459. DOI: 10.1126/science.189.4201.457. eprint: https://www.science.org/doi/pdf/10.1126/science.189.4201.457 (cit. on pp. 9, 10).

Crutzen, Paul J. and Uta Schmailzl (1983). "Chemical budgets of the stratosphere". In: *Planetary and Space Science* 31.9, pp. 1009–1032. ISSN: 0032-0633. DOI: https://doi.org/10.1016/0032-0633(83)90092-2 (cit. on p. 10).

Eriksson, P. (1999). "Microwave Radiometric Observations of the Middle Atmosphere: Simulations and Inversions". In: *PhD thesis. Chalmers University of Technology.* (cit. on p. 33).

Eriksson, P. (2015). "Algorithms Theoretical Basis Document - Level 2 processing". In: *Technical report, Chalmers University of Technology* (cit. on p. 37).

Eriksson, P., S. A. Buehler, C. P. Davis, C. Emde, and O. Lemke (2011). "ARTS, the atmospheric radiative transfer simulator, version 2". In: *Journal of Quantitative Spectroscopy and Radiative Transfer* 112.10, pp. 1551 –1558. ISSN: 0022-4073. DOI: 10.1016/j.jqsrt.2011.03.001 (cit. on p. 37).

Eriksson, P. and J. Urban (2006). "Post launch characterisation of Odin-SMR sideband filter properties". In: *Technical report, Chalmers University of Technology* (cit. on p. 31).

Frisk, U. et al. (2003). "The Odin satellite I. Radiometer design and test". In: *A&A* 402.3, pp. L27–L34. DOI: 10.1051/0004-6361:20030335 (cit. on pp. 29, 31).

Funke, B., M. López-Puertas, S. Gil-López, T. von Clarmann, G. P. Stiller, H. Fischer, and S. Kellmann (2005). "Downward transport of upper atmospheric NOx into the polar stratosphere and lower mesosphere during the Antarctic 2003 and Arctic 2002/2003 winters". In: *Journal of Geophysical Research: Atmospheres* 110.D24. DOI: https://doi.org/10.1029/2005JD006463. eprint: https://agupubs.onlinelibrary.wiley.com/doi/pdf/10.1029/2005JD006463 (cit. on p. 24).

Funke, B., M. López-Puertas, L. Holt, C. E. Randall, G. P. Stiller, and T. von Clarmann (2014). "Hemispheric distributions and interannual variability of NOy produced by energetic particle precipitation in 2002–2012". In: *Journal of Geophysical Research: Atmospheres* 119.23, pp. 13,565–13,582. DOI: https://doi.org/10.1002/2014JD022423. eprint: https://agupubs.onlinelibrary.wiley.com/doi/pdf/10.1002/2014JD022423 (cit. on p. 24).

Funke, B. et al. (2011). "Composition changes after the "Halloween" solar proton event: the High Energy Particle Precipitation in the Atmosphere (HEPPA) model versus MIPAS data intercomparison study". In: *Atmospheric Chemistry and Physics* 11.17, pp. 9089–9139. DOI: 10.5194/acp-11-9089-2011 (cit. on p. 22).

Galand, M., D. Lummerzheim, A. W. Stephan, B. C. Bush, and S. Chakrabarti (2002). "Electron and proton aurora observed spectroscopically in the far ultraviolet". In: *Journal of Geophysical Research: Space Physics* 107.A7, SIA 14–1–SIA 14–14. DOI: https://doi.org/10.1029/2001JA000235. eprint: https://agupubs.onlinelibrary.wiley.com/doi/pdf/10.1029/2001JA000235 (cit. on p. 24).

Ganushkina, N. Yu, I. Dandouras, Y. Y. Shprits, and J. Cao (2011). "Locations of boundaries of outer and inner radiation belts as observed by Cluster and Double Star". In: *Journal of Geophysical Research: Space Physics* 116.A9. DOI: https://doi.org/10.1029/2010JA016376. eprint: https://agupubs.onlinelibrary.wiley.com/doi/pdf/10.1029/2010JA016376 (cit. on p. 24).

Gerber, E.P. et al. (2012). "Assessing and Understanding the Impact of Stratospheric Dynamics and Variability on the Earth System". In: *Bulletin of the American Meteorological Society* 93.6, pp. 845–859. DOI: 10.1175/BAMS-D-11-00145.1 (cit. on p. 5).

Kiviranta, J., K. Pérot, P. Eriksson, and D. Murtagh (2018). "An empirical model of nitric oxide in the upper mesosphere and lower thermosphere based on 12 years of Odin SMR measurements". In: *Atmospheric Chemistry and Physics* 18.18, pp. 13393–13410. DOI: 10.5194/acp-18-13393-2018 (cit. on p. 33).

Lee, J. N., D.L. Wu, G.L. Manney, M.J. Schwartz, A. Lambert, N.J. Livesey, K.R. Minschwaner, H.C. Pumphrey, and W.G. Read (2011). "Aura Microwave Limb Sounder observations of the polar middle atmosphere: Dynamics and transport of CO and H_2O". In: *J. Geophys. Res.* 116.D05110. DOI: doi:10.1029/2010JD014608 (cit. on p. 8).

Lee, K., Z. Li, Y. Kim, and A. Kokhanovsky (2009). "Atmospheric Aerosol Monitoring from Satellite Observations: A History of Three Decades". In: pp. 13–38. ISBN: 978-1-4020-9673-0. DOI: 10.1007/978-1-4020-9674-7_2 (cit. on p. 28).

Lin, Cissi Y. and Yue Deng (2019). "Nitric Oxide in Climatological Global Energy Budget During 1982–2013". In: *Journal of Geophysical Research: Space Physics* 124.1, pp. 782–789. DOI: https://doi.org/10.1029/2018JA025902. eprint: https://agupubs.onlinelibrary.wiley.com/doi/pdf/10.1029/2018JA025902 (cit. on p. 44).

Lorentz, H.A. (1906). "The absoption and emission lines of gaseous bodies". In: *KNAW, Proceedings, 8 II, 1905-1906, Amsterdam*, pp. 591–611 (cit. on p. 35).

Lossow, S. et al. (2019). "The SPARC water vapour assessment II: profile-to-profile comparisons of stratospheric and lower mesospheric water vapour data sets obtained from satellites". In: *Atmospheric Measurement Techniques* 12.5, pp. 2693–2732. DOI: 10.5194/amt-12-2693-2019 (cit. on pp. 8, 9, 15, 43).

Marsh, D. R., M. J. Mills, D. E. Kinnison, J.-F. Lamarque, N. Calvo, and L. M. Polvani (2013). "Climate Change from 1850 to 2005 Simulated in CESM1(WACCM)". In: *Journal of Climate* 26.19, pp. 7372–7391. DOI: 10.1175/JCLI-D-12-00558.1 (cit. on p. 5).

Marsh, D. R., S. C. Solomon, and A. E. Reynolds (2004). "Empirical model of nitric oxide in the lower thermosphere". In: *Journal of Geophysical Research: Space Physics* 109.A7. DOI: https://doi.org/10.1029/2003JA010199. eprint: https://agupubs.onlinelibrary.wiley.com/doi/pdf/10.1029/2003JA010199 (cit. on p. 10).

Masson-Delmotte V., P. et al. (2021). *Climate Change 2021: The Physical Science Basis. Contribution of Working Group I to the Sixth Assessment Report of the Intergovernmental Panel on Climate Change*. Cambridge, United Kingdom and New York, NY, USA: Cambridge University Press. DOI: 10.1017/9781009157896 (cit. on p. 21).

Matzka, J., C. Stolle, Y. Yamazaki, O. Bronkalla, and A. Morschhauser (2021). "The Geomagnetic Kp Index and Derived Indices of Geomagnetic Activity". In: *Space Weather* 19.5. e2020SW002641 2020SW002641, e2020SW002641. DOI: https://doi.org/10.1029/2020SW002641. eprint: https://agupubs.onlinelibrary.wiley.com/doi/pdf/10.1029/2020SW002641 (cit. on p. 25).

McElroy, Michael B. and John C. McConnell (1971). "Nitrous Oxide: A Natural Source of Stratospheric NO". In: *Journal of Atmospheric Sciences* 28.6, pp. 1095

–1098. DOI: 10.1175/1520-0469(1971)028<1095:NOANSO>2.0.CO;2 (cit. on p. 10).

Minschwaner, K. et al. (2010). "The photochemistry of carbon monoxide in the stratosphere and mesosphere evaluated from observations by the Microwave Limb Sounder on the Aura satellite". In: *J. Geophys. Res.*. 115.D13303. DOI: doi:10.1029/2009JD012654 (cit. on p. 8).

Mironova, Irina, Karen Aplin, Frank Arnold, Galina Bazilevskaya, R. Harrison, Alexey Krivolutsky, Keri Nicoll, E. Rozanov, Esa Turunen, and I. Usoskin (Sept. 2015). "Energetic Particle Influence on the Earth's Atmosphere". In: *Space Science Reviews* 194. DOI: 10.1007/s11214-015-0185-4 (cit. on pp. 21–24).

Miroshnichenko, Leonty and Jorge Perez-Peraza (Jan. 2008). "Astrophysical Aspects in the Studies of Solar Cosmic Rays". In: *International Journal of Modern Physics A* 23, pp. 1–141. DOI: 10.1142/S0217751X08037312 (cit. on p. 22).

Mlynczak, Marty et al. (2003). "The natural thermostat of nitric oxide emission at 5.3 ÎŒm in the thermosphere observed during the solar storms of April 2002". In: *Geophysical Research Letters* 30.21. DOI: https://doi.org/10.1029/2003GL017693. eprint: https://agupubs.onlinelibrary.wiley.com/doi/pdf/10.1029/2003GL017693 (cit. on p. 9).

Murtagh, D. et al. (2002). "An overview of the Odin atmospheric mission". In: *Can. J. Phys.* 80.4, 309–319. DOI: 10.1139/p01-157 (cit. on pp. 30, 31).

Nicolet, Marcel (1984). "On the photodissociation of water vapour in the mesosphere". In: *Planetary and Space Science* 32.7, pp. 871–880. ISSN: 0032-0633. DOI: https://doi.org/10.1016/0032-0633(84)90011-4 (cit. on p. 9).

Oberheide, J., M.E. Hagan, A.D. Richmond, and J.M. Forbes (2015). "DYNAMICAL METEOROLOGY | Atmospheric Tides". In: *Encyclopedia of Atmospheric Sciences (Second Edition)*. Ed. by Gerald R. North, John Pyle, and Fuqing Zhang. Second Edition. Oxford: Academic Press, pp. 287–297. ISBN: 978-0-12-382225-3. DOI: https://doi.org/10.1016/B978-0-12-382225-3.00409-6 (cit. on p. 16).

Orsolini, Yvan J., Varavut Limpasuvan, Kristell Pérot, Patrick Espy, Robert Hibbins, Stefan Lossow, Katarina Raaholt Larsson, and Donal Murtagh (2017). "Modelling the descent of nitric oxide during the elevated stratopause event of January 2013". In: *Journal of Atmospheric and Solar-Terrestrial Physics* 155, pp. 50–61. ISSN: 1364-6826. DOI: https://doi.org/10.1016/j.jastp.2017.01.006 (cit. on p. 16).

Parks, G.K. (2015). "Magnetosphere". In: *Encyclopedia of Atmospheric Sciences (Second Edition)*. Ed. by Gerald R. North, John Pyle, and Fuqing Zhang. Second Edition. Oxford: Academic Press, pp. 309–315. ISBN: 978-0-12-382225-3. DOI: https://doi.org/10.1016/B978-0-12-382225-3.00211-5 (cit. on p. 23).

Pérot, Kristell and Yvan J. Orsolini (2021). "Impact of the major SSWs of February 2018 and January 2019 on the middle atmospheric nitric oxide abundance". In: *Journal of Atmospheric and Solar-Terrestrial Physics* 218, p. 105586. ISSN: 1364-6826. DOI: https://doi.org/10.1016/j.jastp.2021.105586 (cit. on pp. 25, 33).

Randall, C. E., V. L. Harvey, C. S. Singleton, S. M. Bailey, P. F. Bernath, M. Codrescu, H. Nakajima, and J. M. Russell III (2007). "Energetic particle precipitation effects on the Southern Hemisphere stratosphere in 1992–2005". In: *Journal of Geophysical Research: Atmospheres* 112.D8. DOI: https://doi.org/10.1029/2006JD007696. eprint: https://agupubs.onlinelibrary.wiley.com/doi/pdf/10.1029/2006JD007696 (cit. on pp. 11, 25).

Randall, C. E., D. E. Siskind, and R. M. Bevilacqua (2001). "Stratospheric NOx enhancements in the Southern Hemisphere Vortex in winter/spring of 2000". In: *Geophysical Research Letters* 28.12, pp. 2385–2388. DOI: https://doi.org/10.1029/2000GL012746 (cit. on p. 25).

Ray, E. A., M. J. Alexander, and J. R. Holton (1998). "An analysis of the structure and forcing of the equatorial semiannual oscillation in zonal wind". In: *Journal of Geophysical Research: Atmospheres* 103.D2, pp. 1759–1774. DOI: 10.1029/97JD02679 (cit. on p. 16).

Rodger, Craig J. and Mark A. Clilverd (2008). "Hiss from the chorus". In: *Nature* 452.7183, pp. 41–42. DOI: 10.1038/452041a (cit. on p. 23).

Rodgers, C.D. (2000). "Inverse methods for atmospheric sounding: Theory and practise". In: *World Scientific Publishing, 1st edition* (cit. on p. 37).

Rozanov, E., M. Calisto, T. Egorova, T. Peter, and W. Schmutz (2012). "Influence of the Precipitating Energetic Particles on Atmospheric Chemistry and Climate". In: *Surveys in Geophysics* 33.3, pp. 483–501. DOI: 10.1007/s10712-012-9192-0 (cit. on pp. 4, 43).

Rydberg, B., P. Eriksson, J. Kiviranta, J. Ringsby, A. Skyman, and D. Murtagh (2017). "Algorithm Theoretical Basis Document: Level 1 Processing". In: *Technical report, Chalmers University of Technology* (cit. on p. 32).

Schoeberl, M.R. and P.A. Newman (2003). "MIDDLE ATMOSPHERE | Polar Vortex". In: *Encyclopedia of Atmospheric Sciences*. Ed. by James R. Holton. Oxford: Academic Press, pp. 1321–1328. ISBN: 978-0-12-227090-1. DOI: https://doi.org/10.1016/B0-12-227090-8/00228-1 (cit. on p. 14).

Schroeder, J. W. R., G. G. Howes, C. A. Kletzing, F. Skiff, T. A. Carter, S. Vincena, and S. Dorfman (2021). "Laboratory measurements of the physics of auroral electron acceleration by Alfvén waves". In: *Nature Communications* 12.1, p. 3103. DOI: 10.1038/s41467-021-23377-5 (cit. on p. 23).

Seppälä, Annika, Katja Matthes, Cora E. Randall, and Irina A. Mironova (2014). "What is the solar influence on climate? Overview of activities during CAWSES-II". In: *Progress in Earth and Planetary Science* 1.1, p. 24. DOI: 10.1186/s40645-014-0024-3 (cit. on pp. 4, 43).

Sheese, P. E., K. Strong, R. L. Gattinger, E. J. Llewellyn, J. Urban, C. D. Boone, and A. K. Smith (2013). "Odin observations of Antarctic nighttime NO densities in the mesosphere and lower thermosphere and observations of a lower NO layer". In: *Journal of Geophysical Research: Atmospheres* 118.13, pp. 7414–7425. DOI: https://doi.org/10.1002/jgrd.50563. eprint: https://agupubs.onlinelibrary.wiley.com/doi/pdf/10.1002/jgrd.50563 (cit. on p. 33).

Shepherd, T.G. (2000). "The middle atmosphere". In: *Journal of Atmospheric and Solar-Terrestrial Physics* 62.17, pp. 1587 –1601. ISSN: 1364-6826. DOI: https://doi.org/10.1016/S1364-6826(00)00114-0 (cit. on p. 14).

Sinnhuber, M., F. Friederich, S. Bender, and J. P. Burrows (2016). "The response of mesospheric NO to geomagnetic forcing in 2002–2012 as seen by SCIAMACHY". In: *Journal of Geophysical Research: Space Physics* 121.4, pp. 3603–3620. DOI: 10.1002/2015JA022284 (cit. on p. 22).

Sinnhuber, M., H. Nieder, and N. Wieters (2012). "Energetic Particle Precipitation and the Chemistry of the Mesosphere/Lower Thermosphere". In: *Surveys in Geophysics* 33.6, pp. 1281–1334. DOI: 10.1007/s10712-012-9201-3 (cit. on pp. 10, 11, 21, 22).

Siskind, David E., C. A. Barth, and III Russell J. M. (Jan. 1998). "A climatology of nitric oxide in the mesosphere and thermosphere". In: *Advances in Space Research* 21.10, pp. 1353–1362. DOI: 10.1016/S0273-1177(97)00743-6 (cit. on p. 11).

Velinov, Peter I.Y., Simeon Asenovski, Karel Kudela, Jan Lastovicka, Lachezar Mateev, Alexander Mishev, and Peter Tonev (2013). "Impact of cosmic rays and solar energetic particles on the Earth´s ionosphere and atmosphere". In: *J. Space Weather Space Clim.* 3, A14. DOI: 10.1051/swsc/2013036 (cit. on p. 22).

Vignon, Etienne and Daniel M. Mitchell (2015). "The stratopause evolution during different types of sudden stratospheric warming event". In: *Climate Dynamics* 44.11, pp. 3323–3337. DOI: 10.1007/s00382-014-2292-4 (cit. on p. 16).

Zafra, R.L. de and G. Muscari (2004). "CO as an important high-altitude tracer of dynamics in the polar stratosphere and mesosphere". In: *J. Geophys. Res.* 109.D06105. DOI: doi:10.1029/2004JD005102 (cit. on p. 8).

Zander, R., H. Leclercq, and L. D. Kaplan (1981). "Concentration of carbon monoxide in the upper stratosphere". In: *Geophysical Research Letters* 8.4, pp. 365–368. DOI: https://doi.org/10.1029/GL008i004p00365. eprint: https://agupubs.onlinelibrary.wiley.com/doi/pdf/10.1029/GL008i004p00365 (cit. on p. 8).